

An Extended Disk Around a Weak-Lined T Tauri Star: Accretion, Infrared Excess, and X-rays from DoAr 21

Eric L. N. Jensen¹, David H. Cohen¹, Marc Gagné², Victoria Swisher¹,

ABSTRACT

As part of a program to understand disk dispersal and the interplay between circumstellar disks and x-ray emission, we present new *Spitzer* photometry, high-resolution optical spectroscopy, and *Chandra* grating x-ray spectroscopy of the weak-lined T Tauri star DoAr 21. DoAr 21 is a strong x-ray emitter, with conflicting evidence in the literature about its disk properties. We show that multiple lines of evidence point to the presence of a low-surface-density inner disk but substantial outer disk around DoAr 21, including weak but broad H α emission (reported here for the first time since the 1950s), polarimetric variability, PAH and H₂ emission, and a strong 24- μ m excess. The 24- μ m emission is slightly resolved by *Spitzer*, indicating a spatial extent of 300–400 AU from the star. ISOCAM data show that DoAr 21 lies in a region of strong, extended PAH and H₂ emission, excited by the nearby B2 star HD 147889. We suggest that the emission from these molecules observed in DoAr 21's disk may be excited by HD 147889 as well, rather than by DoAr 21 itself; the hard external radiation field may also explain why the disk is visible to such large radii. We also present a new high-resolution x-ray grating spectrum from *Chandra*. The x-ray emission is very hard and dominated by continuum emission, and it is well-fit by a multi-temperature, sub-solar abundance thermal model, typical of hard coronal sources. Since there is no evidence for accretion onto DoAr 21, it is intriguing that the density-sensitive forbidden-to-intercombination line ratio in He-like Si is intermediate between the high- and low-density limits, suggesting that even a purely coronal plasma can exceed the low-density limit of this diagnostic. *Should we say anything about TW Hya and BP Tau here? Does the strong UV flux we invoke above affect this diagnostic?*

¹Swarthmore College Department of Physics and Astronomy, 500 College Ave., Swarthmore PA 19081. E-mail ejensen1, vswishe1, dcohen1@swarthmore.edu.

²West Chester University Department of Geology and Astronomy, West Chester, PA 19383

Subject headings: accretion disks — circumstellar matter — stars: coronae — stars: individual (DoAr 21) — stars: pre-main sequence — X-rays: stars

1. Introduction

An open question in early stellar evolution and planet formation is the process and timescale by which stars disperse their protoplanetary disks. Central to this question is the lifetime of the gas component circumstellar disks. The gas dominates the disk mass, but since small dust grains dominate the infrared opacity, dispersal or growth of these grains can significantly reduce or eliminate the excess infrared emission that is often taken to be the primary signature of a circumstellar disk, even if substantial gas is still present.

Related to the question of gas disk survival and evolution is the influence of x-ray emission on the circumstellar gas, and vice versa. T Tauri stars, low-mass pre-main-sequence stars, are often strong x-ray emitters (see, e.g., the review of Feigelson & Montmerle 1999, and references therein). A detailed understanding of the x-ray emission from these young stars is important both for an understanding of early stellar evolution and due to the x-rays' impact on the surrounding environment. T Tauri stars are often surrounded by disks of gas and dust, from which planets presumably form later in the pre-main-sequence phase. The physical state of these disks is strongly influenced by the star's x-ray emission. The x-rays are the dominant source of ionization of the disk (Igea & Glassgold 1999) and they strongly influence the disk chemistry (Maloney et al. 1996). X-ray flares from the young Sun may have produced the isotopic anomalies seen today in meteorites (Feigelson, Garmire, & Pravdo 2002).

Similarly, the presence of circumstellar gas may play a role in shaping or modifying the star's x-ray emission. The models most often proposed for the x-ray emission of T Tauri stars are (broadly) solar-type magnetic activity scaled up by rapid rotation and/or longer convective turnover times, or interaction between a stellar magnetic field and a circumstellar disk, perhaps via accretion. However, neither the details of the magnetic field geometry nor where exactly the x-rays are produced is well established observationally (e.g., Feigelson & Montmerle 1999). The unprecedented x-ray spectral resolution and sensitivity of the *Chandra* x-ray satellite offers an opportunity to place much better constraints on the temperature and density of the x-ray emitting gas, thereby providing potentially important information about the x-ray emission mechanism(s), and about the x-ray radiation field incident on the circumstellar disk.

To date, however, few high-spectral-resolution x-ray observations of pre-main-sequence

stars have been published; even the distances to the nearest star-forming regions result in x-ray fluxes that make high-resolution observations prohibitively long. There are a handful of notable exceptions, however. TW Hya (Kastner et al. 2002) and HD 98800 (Kastner et al. 2004) both lie in the nearby TW Hya association, with a distance of roughly 50 pc and an age of 5–15 Myr (Weintraub et al. 2000, and references therein). The *Chandra* x-ray spectrum of TW Hya yielded a surprisingly low temperature for the x-ray emitting gas, and suggestions of very high densities in the x-ray emitting regions, leading Kastner et al. (2002) to suggest that the x-ray emission is related to accretion from the star’s circumstellar disk. Stelzer & Schmitt (2004) reached a similar conclusion based on density diagnostics in TW Hya’s XMM-Newton spectrum, and also attributed the low iron abundance seen in the x-ray emitting gas to depletion of some elements from the gas phase onto dust grains in the disk. More recently, Schmitt et al. (2005) presented similar evidence for high-density x-ray emitting gas around the classical T Tauri star BP Tau.

In contrast, the x-ray spectra of both HD 98800 (Kastner et al. 2004) and the similarly-aged (~ 10 Myr) PZ Tel (Argiroffi et al. 2004) are quite similar to spectra of older solar-type stars, suggesting that their x-ray activity is, to first order, scaled-up solar activity. Solar-like x-ray activity is also seen in AB Dor (Sanz-Forcada, Maggio, & Micela 2003), which is near or recently arrived on the zero-age main sequence. Notably, TW Hya and BP Tau show clear evidence of active accretion from their circumstellar disks, while the stars with more solar-like x-ray emission do not have disks.¹

Against the backdrop of this previous work, here we present new *Spitzer* photometry and *Chandra* high-resolution grating spectra of the weak-lined T Tauri star DoAr 21 (a.k.a. V2246 Oph, Elias 2-14, VSSG 23, GSS 23, ROXs 8, Haro 1-6, YLW 26, HBC 637). The primary contrast of DoAr 21 with the handful of pre-main-sequence stars previously observed at high x-ray spectral resolution is its youth; DoAr 21 is embedded in the ρ Oph star-forming region, whereas the others (with the exception of BP Tau) no longer lie in regions of active star formation, and all surrounding molecular gas has been dissipated. With an estimated age of $\lesssim 1$ Myr (Figure 1), DoAr 21 is younger than these other stars, and it also shows evidence for an extended but centrally-cleared circumstellar disk (Sec. 2). The central questions here, then, are how much difference the young age and presence of at least some circumstellar material make in the x-ray emission of DoAr 21, and how the high-energy radiation field incident on the disk may influence its properties.

¹Only the southern component (HD 98800 B) of the wide binary pair in HD 98800 has circumstellar material (Koerner et al. 2000), while Kastner et al. (2004) show clearly that the x-ray spectrum they detect and analyze is from the diskless northern component, HD 98800 A.

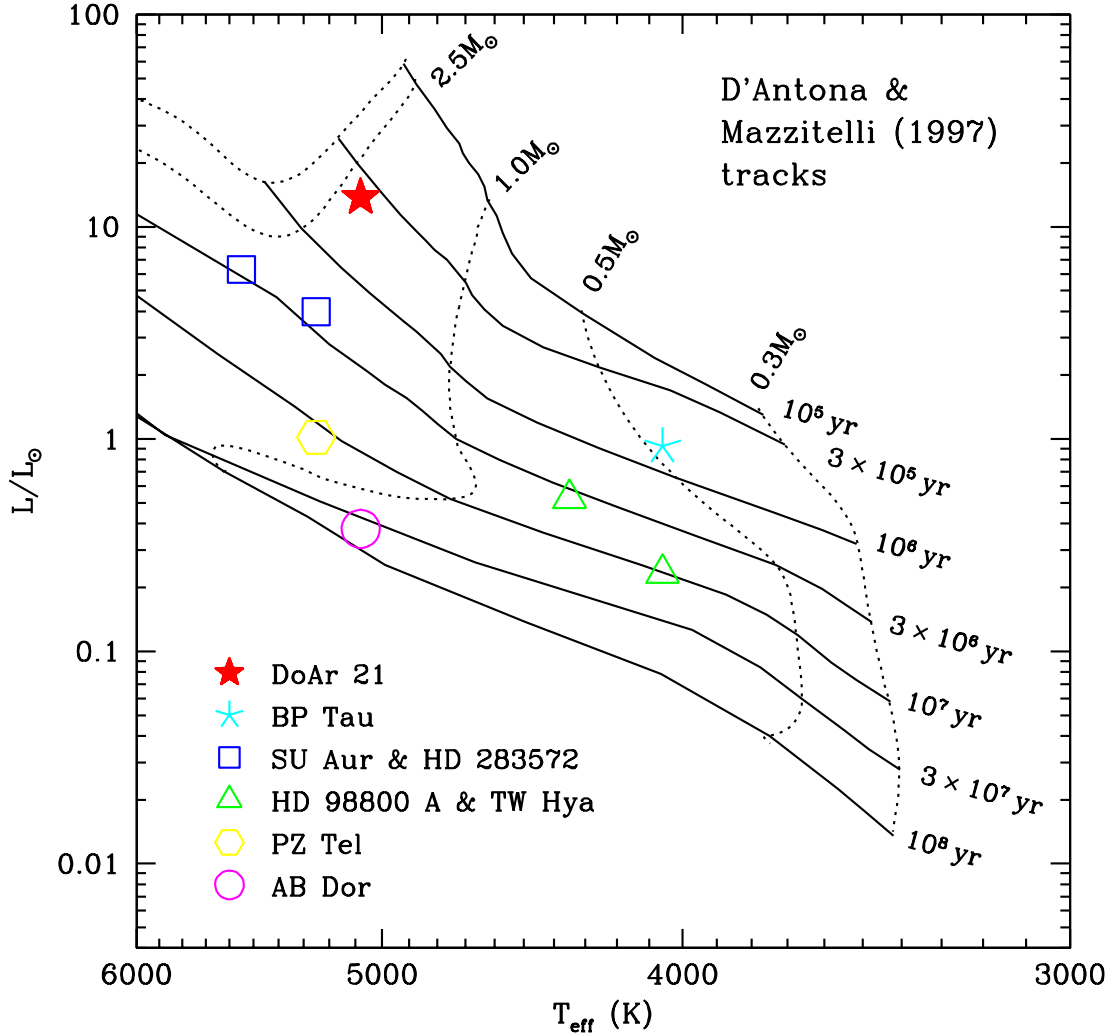


Fig. 1.— HR diagram showing the position of DoAr 21 (filled star) compared to other pre-main-sequence stars that have been observed with the Chandra or XMM-Newton gratings. DoAr 21 is both younger ($\sim 4 \times 10^5$ yr) and more massive ($\sim 2.2 M_{\odot}$) than most of the T Tauri stars observed previously. The pre-main-sequence evolutionary tracks shown are from D’Antona & Mazzitelli (1997). Both the Palla & Stahler (1999) and Siess, Dufour, & Forestini (2000) tracks result in slightly older absolute ages in general, but similar relative ages.

Below we discuss the stellar and circumstellar properties of DoAr 21 (Sec. 2), showing that multiple lines of evidence show the DoAr 21 still retains a circumstellar disk, which, surprisingly, appears in new *Spitzer* images to extend to several hundred AU, but which is not accreting. In this light, we then present our new x-ray observations (Sec. 3) and analyze the x-ray emission in detail through emission-line fits, overall fits to the thermal spectrum, and analysis of time-variability of the emission during a large flare (Sec. 3.3–3.4). In (Sec. 4), we discuss the star’s x-ray emission in the context of its youth and circumstellar environment, arguing that both its disk properties are intermediate between those seen in classical T Tauri stars with optically thick disks, and T Tauri stars that have lost their disks altogether, and that its x-ray emission appears to be wholly coronal. In this light, we examine the robustness of high plasma densities as an argument for a link between accretion and x-ray emission. We also examine whether the presence of a B2 star near DoAr 21 may help explain the detection of extended infrared continuum and molecular gas emission.

2. DoAr 21’s circumstellar environment

Before considering our new x-ray data for DoAr 21, here we consider data from other wavelengths, including new mid-infrared imaging and high-resolution optical spectroscopy. We also consider infrared and optical photometry, spectroscopy, and polarimetry from the literature in order to build up a more complete picture of the circumstellar environment of DoAr 21.

The evidence in the literature for circumstellar material around DoAr 21 (and accretion of such material) is mixed, and DoAr 21 has often been considered (e.g., Lada & Wilking 1984; André et al. 1992; Preibisch 1999; Bontemps et al. 2001) to be a “Class III” or “diskless” T Tauri star, though some sources have stated that it has an infrared excess (e.g., Bouvier & Appenzeller 1992).

In light of the lack of a strong infrared excess, the detection of emission features from polycyclic aromatic hydrocarbons (PAHs; Hanner, Brooke, & Tokunaga 1995) and H₂ (Bary et al. 2003) was surprising, with the latter raising the possibility that a substantial gas component of the disk was still present. Early observations by Haro (1949) and Dolidze & Arakelyan (1959) showed H α in emission. Since then, however, all published spectra of the star have shown H α and Br γ in absorption, and no obvious near-infrared veiling (Bouvier & Appenzeller 1992; Luhman & Rieke 1999; Martín et al. 1998). Our new high-resolution optical spectra (Sec. 2.3) show that the photospheric H α absorption line is partly filled in with emission and is surrounded by weak but very broad (~ 300 km/s FWHM) emission wings, revealing a weak and variable emission component that is consistent with the H α

emission seen in older, coronally-active low-mass stars and which thus suggests that there is little to no accretion onto DoAr 21.

Despite the lack of accretion, we will show below that multiple lines of evidence point to the presence of a circumstellar disk around DoAr 21. The disk appears to have a large radial extent, but it has lower surface density in the inner regions and lacks the accretion seen from disks found around classical T Tauri stars. We will argue that the unusual detection of PAH and H₂ emission features, and the large spatial extent of the 24- μ m emission, may be at least partly a result of the strong UV radiation environment of DoAr 21 in the ρ Oph cloud.

2.1. Spectral energy distribution and infrared excess

2.1.1. Data from the literature

The spectral energy distribution (SED) of DoAr 21 gives some clues to the nature of its circumstellar environment. We searched the literature for available photometry of DoAr 21, and assembled the SED from $\lambda = 0.39 \mu\text{m}$ (U band) to $\lambda = 24 \mu\text{m}$. Spectral types in the literature are K0 (Bouvier & Appenzeller 1992; Martín et al. 1998) from optical spectra and K0–K2 (Luhman & Rieke 1999) from near-infrared spectra. Following Luhman & Rieke (1999), we adopt a spectral type of K1 and effective temperature of 5080 K. The observed broad-band colors are much redder than photospheric colors for a K1 star; Luhman & Rieke (1999) find J -band extinction $A_J = 1.6$ mag, which we adopt here. Using the extinction law of Fitzpatrick (1999), this gives a visual extinction of $A_V = 6.3$ mag, similar to the $A_V = 6.6$ found by Bouvier & Appenzeller (1992). We note that this is self-consistent with the neutral hydrogen column density of $N_H \approx 10^{22}$ atoms cm^{-2} found from the x-ray spectrum (Sec. 3) ; from a sample of 20 sources with good x-ray and infrared data in the ρ Oph cloud, Vuong et al. (2003) find $N_H/A_J = 5.6 \pm 0.4 \times 10^{21} \text{ cm}^{-2} \text{ mag}^{-1}$.

To determine whether or not DoAr 21 shows any evidence of infrared excess, a signature of the presence of a circumstellar disk, we compared the SED of DoAr 21 to a model photosphere (Buser & Kurucz 1992) with $T_{\text{eff}} = 5000$ K (Figure 2). The photometric data have been de-reddened using the extinction law of Fitzpatrick (1999) with $A_V = 6.3$ magnitudes and a ratio of total-to-selective extinction $R_V \equiv \frac{A_V}{E(B-V)} = 4.2$. The value of R_V was determined from the relationship $R_V = 5.7\lambda_{\text{max}}$ (Vrba et al. 1993), where $\lambda_{\text{max}} = 0.74 \mu\text{m}$ is the wavelength of maximum observed polarization for DoAr 21 (Martin et al. 1992). This value of R_V is consistent with results found for other lines of sight in Ophiuchus (Vrba et al. 1993) and yields a notably better fit to the $UBVRI$ data than the standard interstellar value of $R_V = 3.1$.

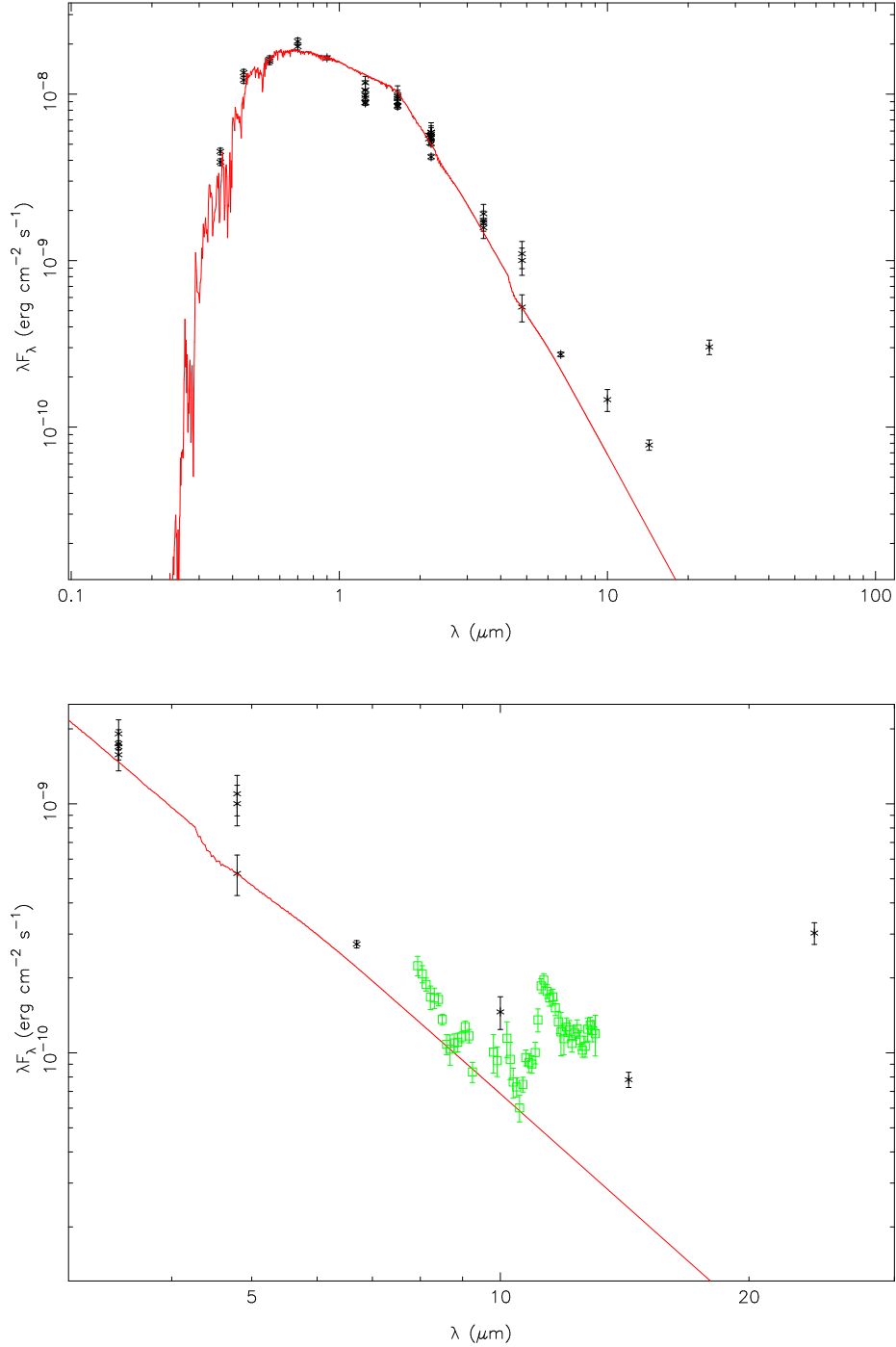


Fig. 2.— Top: The spectral energy distribution of DoAr 21, from ultraviolet through infrared wavelengths. The photometry has been de-reddened with $A_V = 6.3$ and $R_V = 4.2$ as described in the text. Overplotted is a model photosphere (solid line); the star shows a clear infrared excess at $\lambda \geq 10$ μ m. Bottom: A close-up of the mid-infrared spectrum, showing the broad-band measurements from above, but also showing data from Hanner, Brooke, & Tokunaga (1995) (squares, red in the on-line edition) which show emission features attributed to polycyclic aromatic hydrocarbons (PAHs).

While the observed optical and near-infrared variability (see Section 2.2) makes it impossible to fit every data point, the photometry is broadly consistent with the model photosphere within the uncertainties for $\lambda \leq 3 \mu\text{m}$. There is some evidence for excess emission at U and B , which could be due to flaring as discussed below. However, while the brightest U and B points are clearly inconsistent with photospheric emission, these short-wavelength points are the most sensitive to the determination of the extinction (both its absolute level and its wavelength dependence), and the U photometry has the largest uncertainties, so the presence of a short-wavelength excess in the fainter U and B points is not secure.

Far more robust, however, is the presence of a clear infrared excess at $\lambda = 7\text{--}14 \mu\text{m}$. These points are quite insensitive to extinction corrections, since the extinction is so small, and to the determination of the star’s effective temperature, since they lie on the Rayleigh-Jeans tail of the photospheric emission. The $\lambda = 6.7$ and $14 \mu\text{m}$ points are ISO data from Bontemps et al. (2001), and the $\lambda = 10 \mu\text{m}$ point is from Lada & Wilking (1984). While the presence of an excess at 4.8 or $6.7 \mu\text{m}$ is debatable, the $10\text{--}14 \mu\text{m}$ points are well in excess of the photospheric emission, indicating the presence of some circumstellar disk material.

2.1.2. *Spitzer photometry*

DoAr 21 was observed by the *Spitzer Space Telescope* with the MIPS instrument, at wavelengths of 24 , 70 , and $160 \mu\text{m}$. Figure 3 shows the $\lambda = 24 \mu\text{m}$ image of the region around DoAr 21; DoAr 21 itself is clearly detected. Visual examination of the $70\text{-}\mu\text{m}$ images shows some suggestion of a source at the position of DoAr 21, but the noise is too high for a definitive detection.

We carried out aperture photometry of DoAr 21 on the mosaicked, post-baseline-calibrated $24\text{-}\mu\text{m}$ images, using an aperture size of 6 pixels and aperture correction of 0.87719 (Hines et al. 2005). This yields a flux of $2.3 \pm 0.2 \text{ Jy}$ at $\lambda = 24 \mu\text{m}$, where the uncertainty is dominated by the 10% absolute calibration uncertainty of MIPS (Hines et al. 2005).

When plotted on the spectral energy distribution (Figure 2), this point shows a large infrared excess, laying to rest any doubts about the presence of a disk around DoAr 21. The dramatic jump in excess emission from 14 to $24 \mu\text{m}$ is consistent with a relatively sparse inner disk, but larger disk surface density at radii larger than a few AU. We discuss possible disk geometries further in Section 4.

Surprisingly, the $24\text{-}\mu\text{m}$ emission from DoAr 21 appears to be somewhat extended. Close inspection of the $24\text{-}\mu\text{m}$ MIPS images reveals that the profile of DoAr 21 is different from that of other stars in the field. Since *Spitzer* is diffraction-limited at $24 \mu\text{m}$, the point-

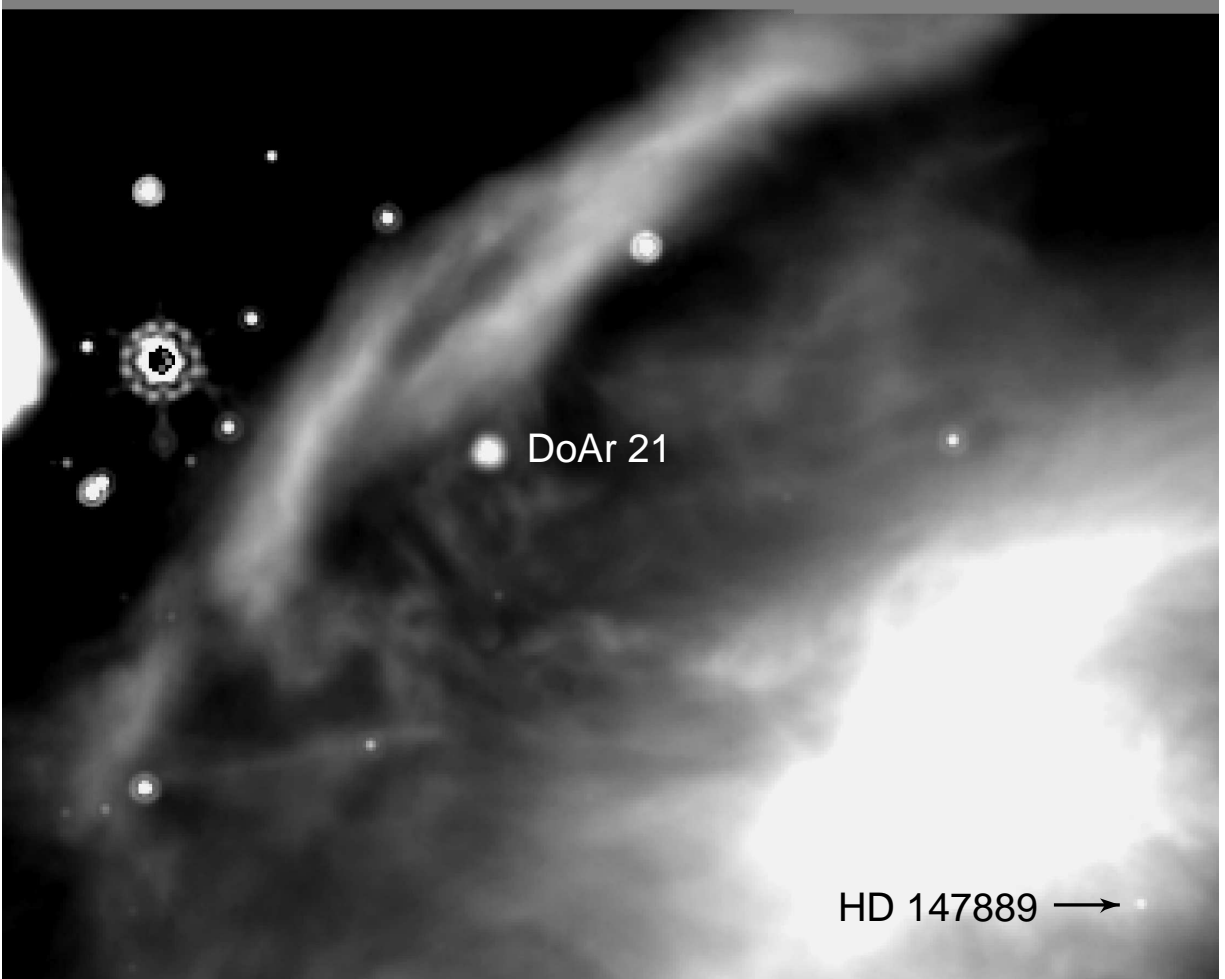


Fig. 3.— *Spitzer* MIPS 24- μm image of the field around DoAr 21. DoAr 21 is clearly detected, indicating a substantial amount of circumstellar material. Unlike other stellar sources in the field, DoAr 21 does not show the first Airy ring, indicating that the 24- μm emission is marginally resolved.

spread-function (PSF) is a modified Airy pattern, and indeed many of the sources in Figure 3 (including sources that are fainter than DoAr 21 and/or projected on comparable or brighter background emission) show the presence of the first Airy ring. DoAr 21 does not, however, indicating that it is not a point source at $24\ \mu\text{m}$. This can be seen more clearly in Figure 4, which shows the azimuthally-averaged radial profile of DoAr 21 compared to that of a star in the same image (GSS 26), and also to a sample empirical on-orbit PSF (constructed from many stars in a MIPS mosaic image of the Trapezium) supplied by the Spitzer Science Center. DoAr 21 is clearly more extended than the other stars, both of which show the signature of the first Airy ring at radii of 3–5 pixels. (The diffraction limit of *Spitzer* at $24\ \mu\text{m}$ is $7''.4$, while the MIPS mosaic pixel size is $2''.45$, so the first null occurs at a radius of 3 pixels.) We examined three different MIPS mosaic images, and DoAr 21 appears extended in all of them. We also examined the individual baseline-calibrated (BCD) data frames from the SSC archive (from which the mosaics were constructed), and found that DoAr 21 appears extended in each frame, regardless of its position on the chip, while other stars in the frame do not. Thus, the broader profile of DoAr 21 is not an artifact of the mosaicking process.

To estimate the radial extent of the emission, we convolved an oversampled MIPS PSF with Gaussians of different radii, resampled them at the MIPS pixel scale, and compared their radial profiles to that of DoAr 21. The results are shown in Figure 5. The profile of DoAr 21 is roughly consistent with a Gaussian source with a sigma of 0.75–1 MIPS pixel. At the 140 pc distance of DoAr 21, this corresponds to a FWHM of 600–800 AU. Thus, the $24\text{-}\mu\text{m}$ emission appears to be extended to radii of 300–400 AU from the star. We discuss possible explanations for this surprising result in Section 4.

2.2. Photometric and Polarimetric Variability

Multiple measurements exist at wavelengths from $0.39\ \mu\text{m}$ (U) through $4.8\ \mu\text{m}$ (M). Variability is seen at all wavelengths. The range at V band in 15 measurements is 0.33 magnitudes, with variations on timescales of less than one day, but with no apparent periodicity (Bouvier et al. 1988). Substantial variability is seen in the ultraviolet; in two observations separated by less than an hour, Bouvier et al. (1988) observed a brightening of 0.97 magnitudes in U , while B brightened by 0.03 magnitudes and V faded by 0.02 magnitudes. Two observations separated by 3 hours on the following night showed a similar variation, with U brightening by 0.42 magnitudes while B and V faded by 0.04 and 0.05 magnitudes, respec-

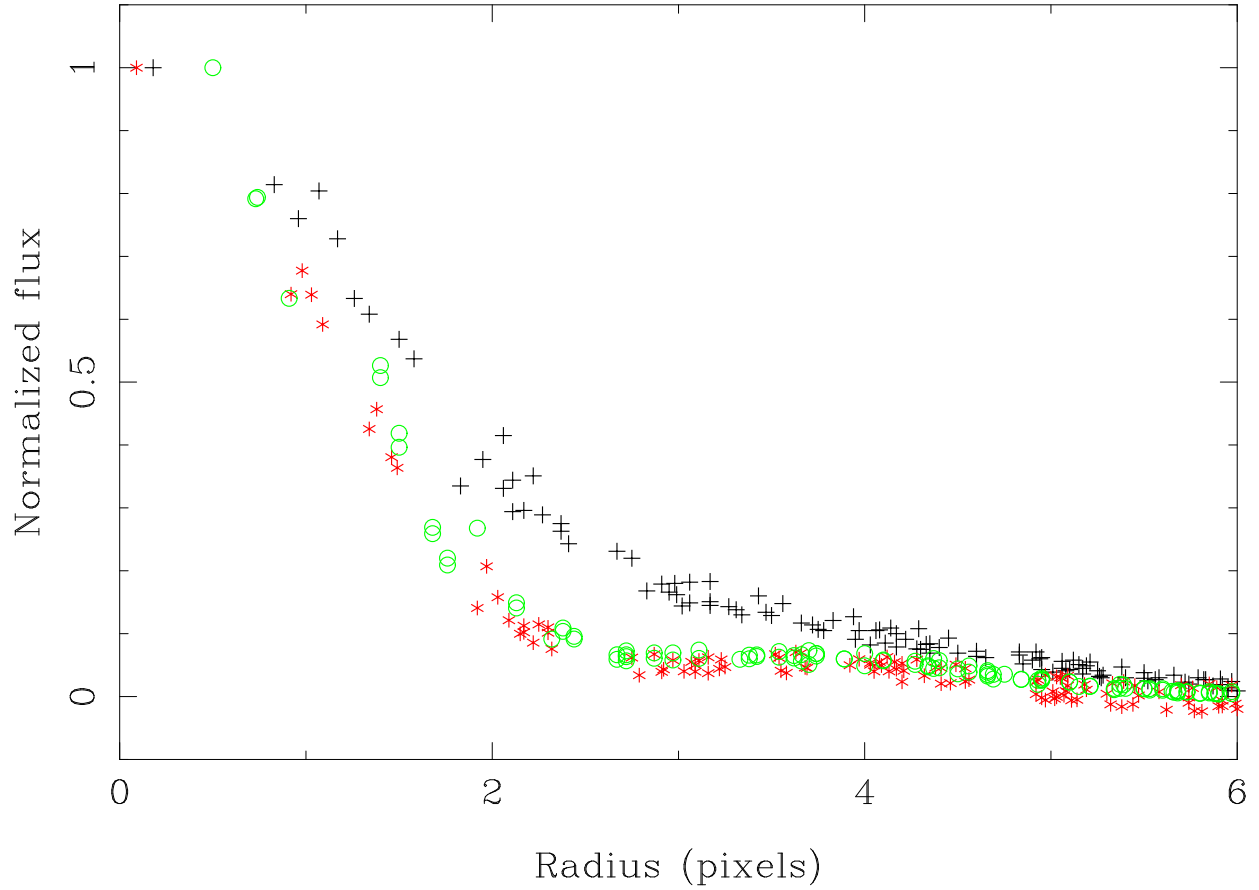


Fig. 4.— Azimuthally-averaged radial profiles of stars observed by *Spitzer* with MIPS at $24\ \mu\text{m}$. DoAr 21 (crosses) is slightly extended compared to another star in the same field (circles; green in the on-line edition) or a composite PSF from a different field (asterisks; red in the on-line edition), both of which show the expected diffraction pattern for a point source.

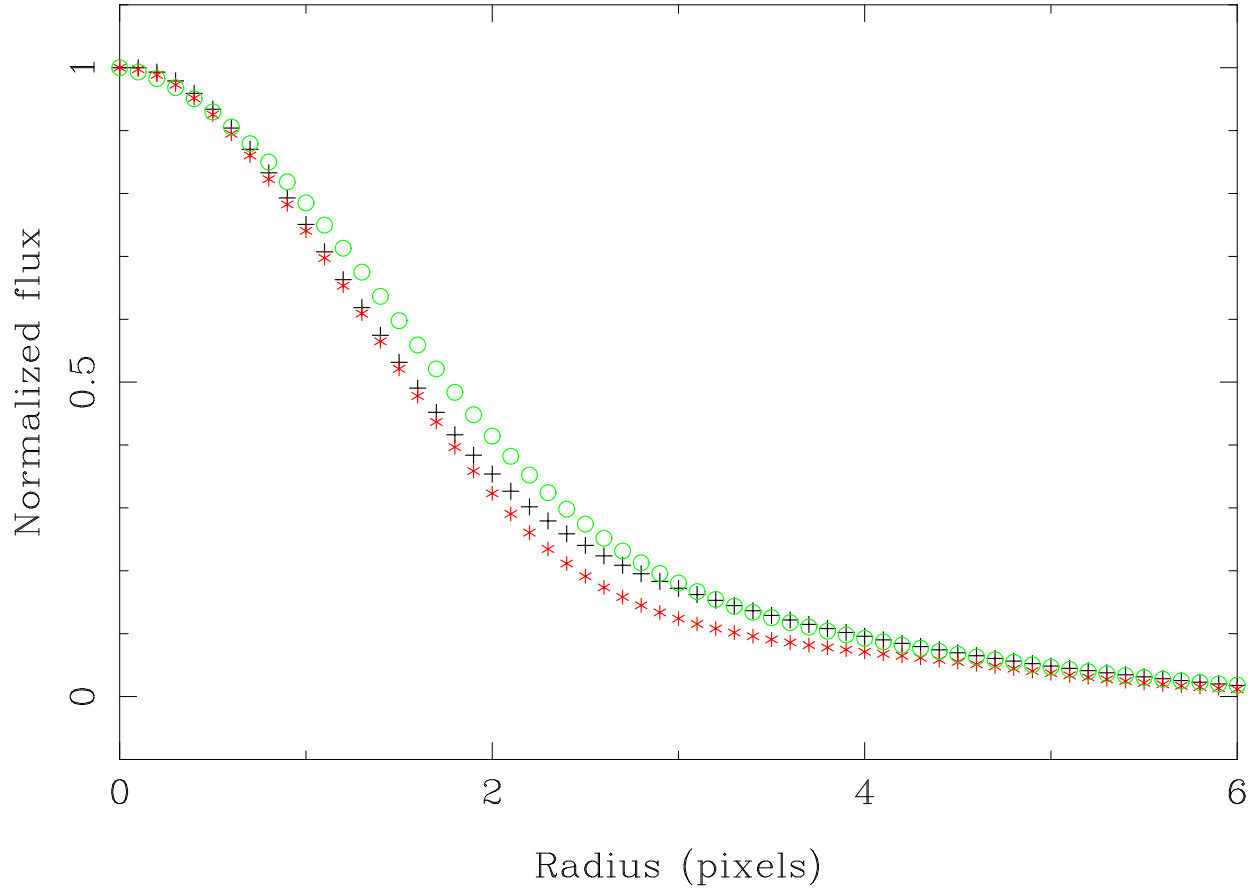


Fig. 5.— DoAr 21’s radial profile at $24\ \mu\text{m}$ (crosses) compared to Gaussians of different widths convolved with the MIPS PSF. DoAr 21 appears to be consistent with a Gaussian having a sigma of 0.75 (asterisks; red in the on-line edition) to 1 (circles; green in the on-line edition) MIPS $2''.45$ pixels, indicating a radial extent of 300–400 AU. For ease of comparison, the plot shows spline fits to the empirical radial profiles.

tively.² Such a large increase in the UV emission without a concurrent increase in V cannot be due to rotational modulation (either of hot or cool spots), since that would increase the flux in all bands (e.g., Rydgren & Vrba 1983). These U -band brightenings are similar to flares seen on active main-sequence stars in that they are much brighter at U than at V (Fernández et al. 2004). We note that both of these brightening events occur when the star is at the faint end of the observed U range, i.e. they are brightenings toward the mean value rather than above it. This may simply indicate that the star is flaring much of the time and that the observed mean value in the data of Bouvier et al. (1988) is characteristic of the flares rather than the photosphere. The U and B magnitudes are positively correlated with each other (with a larger amplitude at U), but neither the U or B magnitudes nor the $U - B$ color is correlated with V .

The bluest observed $U - B$ color for DoAr 21 in the photometry of Bouvier et al. (1988) is $U - B = 0.5$, observed on two consecutive nights. Using our adopted extinction, the de-reddened color is $(U - B)_0 \approx -0.5$. This has a color temperature of $T \approx 14,000$ K (Schmidt-Kaler 1982), similar to (though slightly hotter than) the 8,000–11,000 K temperatures typically deduced for accretion-related veiling emission in classical T Tauri stars from optical or ultraviolet spectra (e.g., Valenti, Basri, & Johns 1993).

We conclude that the existing photometric data are not sufficient to clearly differentiate between variability due to episodic accretion vs. that from flaring similar to that seen on chromospherically-active main-sequence stars. Indeed, both may be occurring at some level.

Can we say anything useful about UV emission from x-ray flares here?

DoAr 21’s K -band emission is polarized at $p \approx 2\%$ (Martin et al. 1992). The large visual extinction toward DoAr 21 suggests that this could be attributed to interstellar polarization from overlying cloud material not closely associated with the star. However, the polarization is variable both in amplitude and in position angle (Jensen et al. 2004). Since the foreground cloud is not expected to change on short timescales, this variability suggests a circumstellar origin for DoAr 21’s polarization, further evidence for the presence of some disk material.

²Bouvier et al. (1988) do not give error bars on individual measurements. They quote typical errors of 0.09, 0.06, and 0.04 mags for U , B , and V for a $V = 12$ star; DoAr 21 is $V \approx 14$. Observations of other stars with similar V magnitudes observed during the same nights as the U flares on DoAr 21 do not show U magnitudes that are substantially different from the mean values for those stars, suggesting that the observed changes at U in DoAr 21 are real, and not photometric errors.

2.3. Optical spectrum

We observed DoAr 21 with the echelle spectrograph on the CTIO Blanco 4-meter telescope on 2002 June 12 and 14, and on the four consecutive nights 2003 April 11–14. The spectrograph setup gave wavelength coverage of approximately 5,000–8,000 Å with 0.08 Å/pixel. With a 1" slit width, this gave a spectral resolution (as measured from the FWHM of narrow lines in a ThAr comparison lamp spectrum) of $R = 40,000$ at the H α line. Exposure times were 20 minutes on 2002 June 12, 15 minutes on 2003 April 11 and 30 minutes on the other four nights. The data were reduced using standard routines for echelle spectra in IRAF.³

Comparison of these spectra with a K1 V standard spectrum artificially broadened to various velocities gives a projected rotational velocity $v \sin i = 80 \pm 10 \text{ km s}^{-1}$ for DoAr 21.⁴ Combined with an estimate of DoAr 21's radius from its effective temperature and luminosity, this gives a rotational period of around 2 days, or less if the star is not viewed equator-on.⁵ Thus, it is possible that Bouvier et al. (1988) did not observe rotationally-modulated variability because their sampling was too infrequent. To our knowledge, there has been no concerted photometric monitoring campaign on DoAr 21 that would be sensitive to such short rotational periods.

DoAr 21 has at times shown H α in emission in the past (Haro 1949; Dolidze & Arakelyan 1959), while other observations have shown H α absorption. Our observations, shown in Figure 6, show a combination of both. There is a central photospheric absorption line, but our high spectral resolution reveals the presence of broad emission wings. In addition, comparison with the K1 V spectral standard HD 13445 (Keenan & McNeil 1989), artificially broadened to $v \sin i = 80 \text{ km s}^{-1}$, shows that DoAr 21's H α absorption line is substantially

³IRAF is distributed by the National Optical Astronomy Observatories, which are operated by the Association of Universities for Research in Astronomy, Inc., under cooperative agreement with the National Science Foundation.

⁴Massarotti et al. (2005) report $v \sin i = 29 \text{ km s}^{-1}$ for DoAr 21. The origin of the discrepancy between their determination and ours is unclear. The CfA spectra, measured at similar spectral resolution but with less spectral coverage and lower S/N, show some variation in the width of the cross-correlation peak, which is a measure of the line width, occasionally showing broader peaks that are consistent with higher $v \sin i$ (D. Latham, personal communication). Our spectra show consistently broad lines, and none of our six spectra is consistent with $v \sin i$ as low as 29 km s^{-1} . We repeated the procedure used by Massarotti et al. (2005) on our spectra, cross-correlating various artificially broadened template spectra with DoAr 21 to find the template that gives the highest correlation peak, and we consistently find $v \sin i \approx 80 \text{ km s}^{-1}$.

⁵Bary et al. (2003) suggest that the inclination DoAr 21 is greater than 55° . If this is the case, then the equatorial rotational velocity is greater than 100 km s^{-1} .

filled in with emission.

Further, the line varies substantially from one night to the next. Figure 6b shows the difference between two nights, clearly showing the presence of a broad, variable emission component at $H\alpha$. The emission shown here is a lower limit to the true $H\alpha$ emission line flux, since any emission component present on both nights is subtracted out. The FWHM of the emission is $\sim 300 \text{ km s}^{-1}$, while the full width at 10% intensity is $\sim 450 \text{ km s}^{-1}$. White & Basri (2003) propose that stars with $H\alpha$ full width at 10% intensity of $> 270 \text{ km s}^{-1}$ should be considered classical T Tauri stars, arguing that the line velocity width is a better accretion diagnostic than the more commonly used equivalent width. By this measure, DoAr 21 could be considered to be a classical (accreting) T Tauri star, and indeed this is consistent with some of the evidence, including the infrared excess, the H_2 emission (Bary et al. 2003), and the polarimetric variability.

However, some stars that are not thought to be accreting show $H\alpha$ behavior similar to that seen in DoAr 21. Montes et al. (1997) find that some chromospherically active binary stars show $H\alpha$ emission that is well-fit by a broad component and a narrow component, with the broad component having FWHM values from 133 to 470 km s^{-1} . Fernández et al. (2004) find that the quiescent (non-flare) spectrum of the weak-lined pre-main-sequence triple system V410 Tau has $H\alpha$ that is just filled in, not overtly in emission, while during a flare the $H\alpha$ equivalent width is 27 Å. After subtraction of a photosphere of the correct spectral type from the quiescent spectrum, they find that the residual $H\alpha$ emission line (equivalent width $\sim 1 \text{ Å}$, similar to the emission component from DoAr 21) has a broad component with a FWHM of 300-400 km s^{-1} . During a flare, the $H\beta$ line is observed to be in emission with FWHM of 730 km s^{-1} , with its width declining as the flare decays. V410 Tau shows no evidence of infrared excess or other indicators of accretion, though definitive detection of a weak infrared excess would be difficult given the shortage of resolved infrared measurements of the three stars (all within $0''.3$; White & Ghez 2001) in the system. Given the lack of evidence for a disk, the $H\alpha$ seems more likely to be related to the flares than to accretion. Apparently broad Balmer emission lines are not by themselves an unambiguous indicator of accretion.

2.4. Optical Imaging

Archival WFPC/2 images of DoAr 21 in the F606W and F814W filters show a faint filament extending southeast from the star; the filament is not apparent in images in the F1042M filter. There is no obvious brightness gradient along the filament, so Stapelfeldt et al. (2005) suggest that it is foreground or background material illuminated by the star,

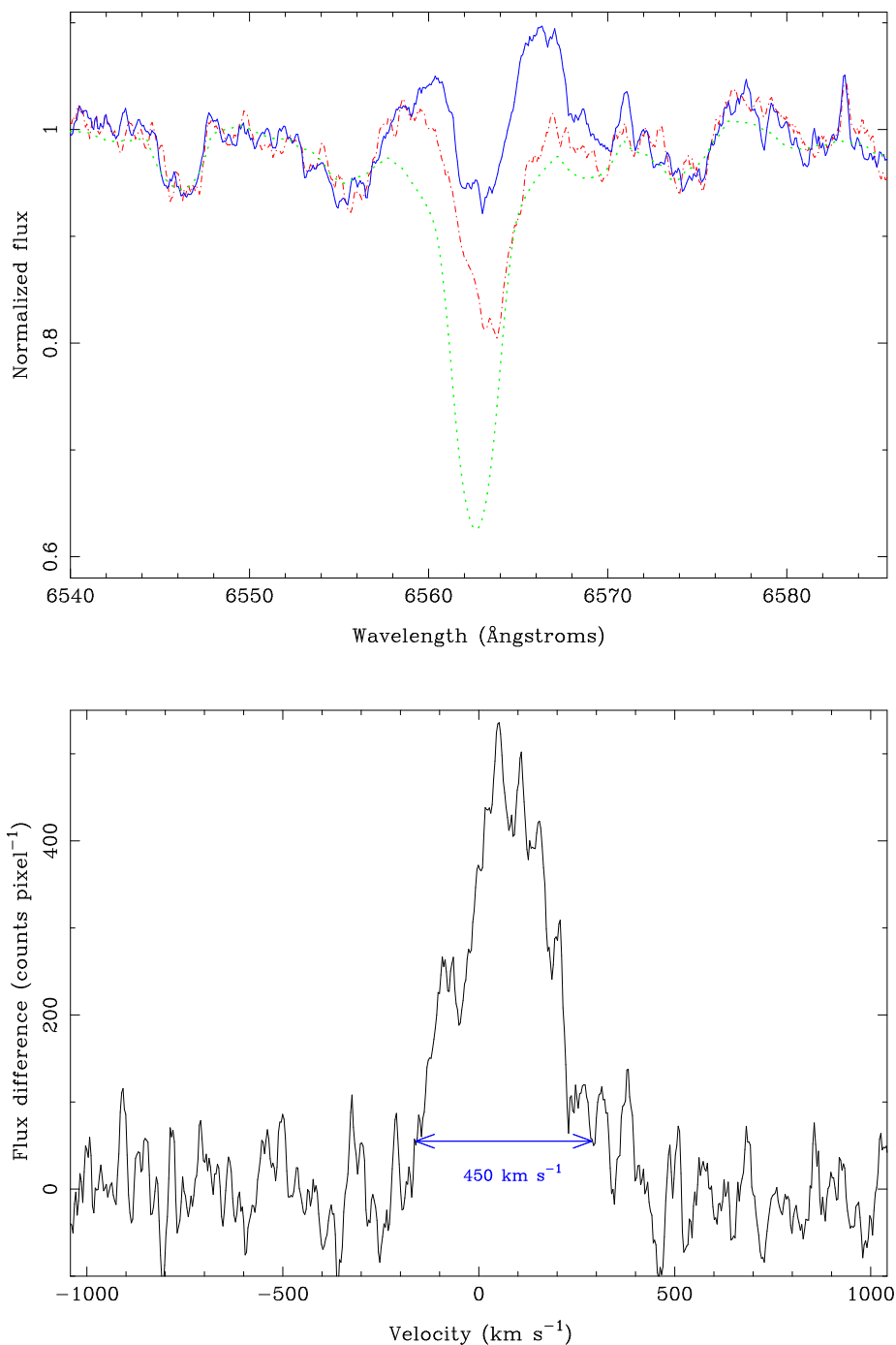


Fig. 6.— High-resolution optical spectra of DoAr 21 in the vicinity of the $H\alpha$ line. Top: The dot-dashed line (red in the online edition) shows DoAr 21 on 12 April 2003; the solid line (blue in the online edition) shows DoAr 21 on 13 April 2003; the dotted line (green in the online edition) shows the K1 V standard star HD 13445, artificially broadened to $v \sin i = 80 \text{ km s}^{-1}$. The $H\alpha$ line in DoAr 21 clearly is filled in by a broad emission component that is present on both nights, but stronger on the second night. Bottom: The difference between the two DoAr 21 spectra, showing the broad emission component that appears the second night. The full-width at 10% intensity is indicated.

rather than a jet reaching near the stellar surface.

2.5. PAH Emission

Further evidence for a circumstellar disk is shown in Figure 2b, which shows the mid-infrared spectrum of DoAr 21 from Hanner, Brooke, & Tokunaga (1995) along with the model photosphere. As with the broad-band points, these data lie well above the photosphere. In addition, they show a clear emission feature at $\lambda = 11.2 \mu\text{m}$, attributed by Hanner, Brooke, & Tokunaga (1995) to emission from polycyclic aromatic hydrocarbons (PAHs).

DoAr 21 was also observed by ISO with the circularly-variable filter (CVF) on ISOCAM, yielding a $\lambda/\Delta\lambda \approx 50$ –80 spectrum from 5.1–16.6 μm of DoAr 21 and its surroundings with 6'' pixels. These data were reprocessed by Boulanger et al. (2005) as part of the final reprocessing of all ISOCAM CVF data, and we retrieved the reprocessed data from the ISO archive. The data show a strong point source at the position of DoAr 21, as well as a bright ridge of emission located 30''–90'' NE of DoAr 21 and running NW–SE; this ridge is clearly visible in the *Spitzer* 24- μm image as well (Figure 3) and can also be seen faintly in the 2MASS K-band images. All pixels in the ISOCAM 3'3 x 3'3 field of view show a rich PAH spectrum, including emission features at 6.2, 7.7, 8.6, 11.3, and 12.7 μm (Figure 7).

Unfortunately, it is not possible to determine a reliable spectrum for DoAr 21 itself from these data. Due to internal reflections in ISOCAM when used with the CVF, the spectrum of DoAr 21 is contaminated by “ghosts”, reflections of stray light from elsewhere in the field of view (Okumura et al. 1998). This is revealed by sharp discontinuities in the spectrum of DoAr 21 around 9 μm , the transition wavelength between CVF1 and CVF2. The ghosts are significantly worse in CVF2, and this discontinuity is a signature of stray light contamination (Boulanger et al. 2005). We suspect that the contamination arises from the bright ridge of emission to the NE of DoAr 21, which is of the same order of magnitude in brightness at these wavelengths as DoAr 21 itself. Because the background emission is diffuse and spatially variable, and the ghost size and strength are functions of wavelength, it is not possible to reconstruct the uncontaminated spectrum of DoAr 21 from these data.

Nonetheless, the spectrum observed by Hanner, Brooke, & Tokunaga (1995) shows PAH emission in a 5'' aperture at the position of DoAr 21. What is the origin of this emission? Given that PAH emission appears throughout the DoAr 21 field, is the PAH emission near DoAr 21 itself excited by the star, or by the same mechanism that excites the surroundings? Emission from small, neutral PAH grains requires excitation by UV photons, and thus Hanner, Brooke, & Tokunaga (1995) suggested that the observed PAH emission

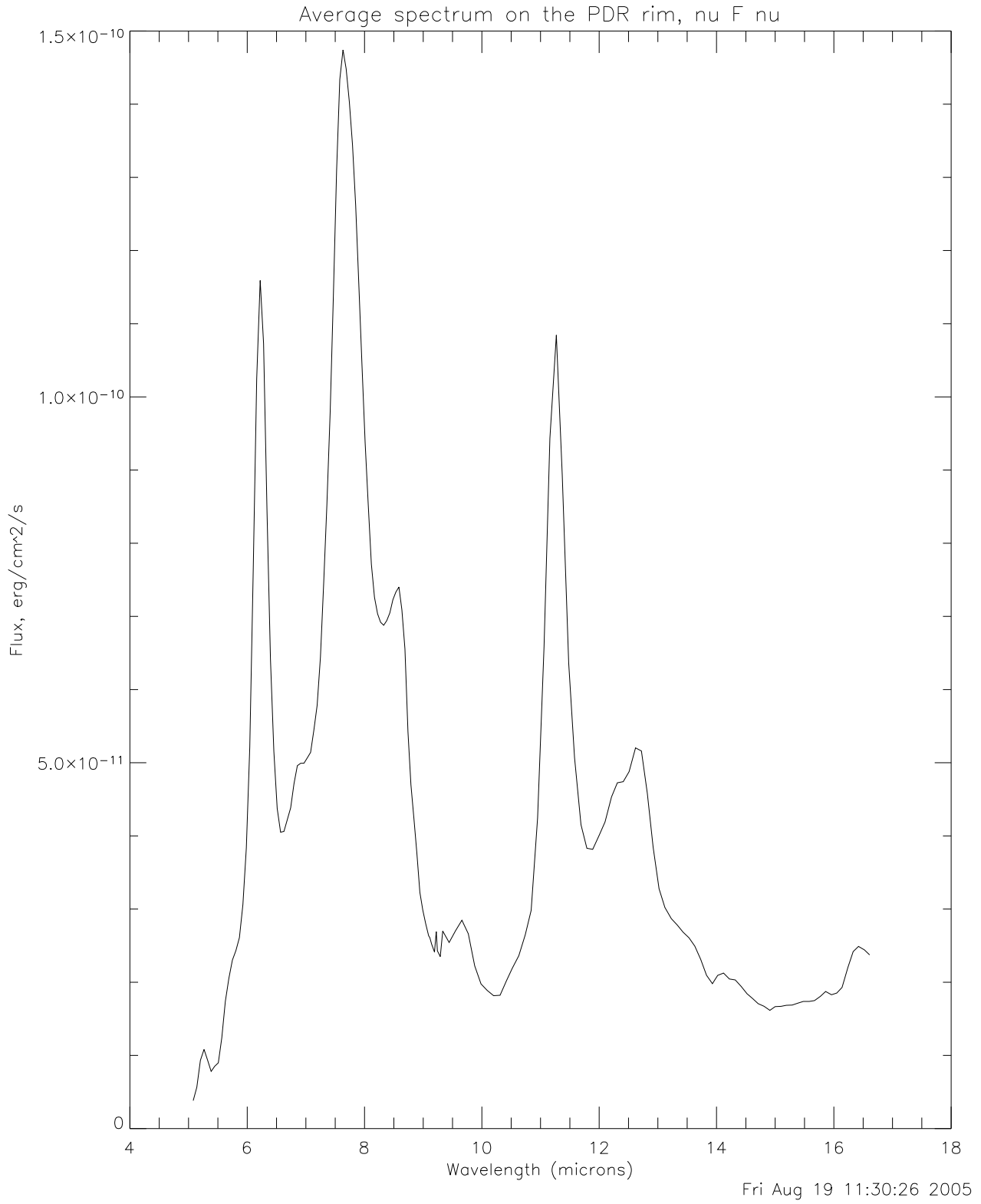


Fig. 7.— Spectrum of the infrared background emission near DoAr 21, from ISOCAM CVF. A rich spectrum of PAH features is present, as well as the $\lambda = 9.66 \mu\text{m}$ 0-0 S(3) H₂ feature.

could not be excited by DoAr 21 itself. They hypothesized that the PAH emission observed at the position of DoAr 21 may be excited by the B2 V star HD 147889, 10' to the SW (Figure 3), the illuminating source of the bright rim of nebulosity near DoAr 21. We return below to discussion of the role that HD 147889 may play in influencing the emission from DoAr 21.

A question here: the Spitzer IRAC 4 images (and to some extent the ISO images) show that the background emission is clearly variable on the 30' scales that Hanner et al. used for their chop throw for sky subtraction, raising the possibility that the PAH emission they observed is simply contamination from the nebulosity, and not from DoAr 21 at all. Do you think we should bring that up here?

2.6. H₂ emission

As noted above, Bary et al. (2002, 2003) detected H₂ emission from DoAr 21, further evidence of a substantial amount of circumstellar material. As in the case of the PAH emission, additional data show that H₂ emission is a ubiquitous feature of the surroundings of DoAr 21. The ISOCAM CVF data discussed in Section 2.5 show the presence of the $\lambda = 9.66 \mu\text{m}$ 0–0 S(3) H₂ feature at many locations in the DoAr 21 field. In addition, Habart et al. (2003) conducted ground-based narrow-band imaging, showing that the bright bar NE of DoAr 21 (seen in both the *Spitzer* and ISO images) is also bright in the H₂ 1–0 S(1) line, the same transition detected by Bary et al. (2003) in DoAr 21. The imaging observations do not include the position of DoAr 21 itself, but they extend to within about 40'' of it, covering the bright rim immediately to the north. Further, Habart et al. (2003) show that the PAH emission seen by ISOCAM in this region correlates very well in strength and position with the H₂ 1–0 S(1) emission seen in the ground-based images, and with the H₂ 0–0 S(3) emission seen by the ISO SWS. Thus, it is quite plausible that the H₂ 1–0 S(1) emission follows the PAH and H₂ 0–0 S(3) emission in the region immediately surrounding DoAr 21 as well. The presence of extended H₂ emission does not suggest that there is not also H₂ in the immediate circumstellar environment of DoAr 21 as well; Bary et al. (2002) subtracted the background emission and found a clear detection of H₂ 1–0 S(1) emission confined to a position with 1''4 of DoAr 21 itself. From the resolved velocity width of the line, they also argued that the gas must reside in a rotating circumstellar disk. What the presence of extended emission does indicate, however, is that the conditions for exciting strong H₂ (and PAH) emission exist throughout the region around DoAr 21, not just in the immediate circumstellar environment.

3. X-ray emission

In light of the strong evidence for a disk around DoAr 21, its rapid rotation, and indications that high-energy photons play an important role in the circumstellar environment, we now turn to an examination of the x-ray data for DoAr 21. As noted in Section 1, there is spectroscopic evidence that accretion may be related to x-ray emission in T Tauri stars. We present below a new high-resolution x-ray spectrum of DoAr 21, but first we discuss briefly the previous work on DoAr 21’s x-ray and magnetic activity.

DoAr 21 shows strong magnetic activity. Its non-thermal radio emission is marginally resolved with a size of order 10 stellar radii (Phillips, Lonsdale, & Feigelson 1991) and has been observed to vary rapidly (Stine et al. 1988). It is also one of the strongest x-ray sources in the Ophiuchus molecular cloud (Casanova et al. 1995). A 38-ksec ASCA observation showed a very hard x-ray spectrum but no variability (Koyama et al. 1994), while a 100-ksec *Chandra* ACIS observation showed DoAr 21 to be in the decay phase of a large flare (Gagné, Skinner, & Daniel 2004).

The strong activity of DoAr 21 has been attributed in the literature to the fact that DoAr 21 supposedly does not have a disk and therefore may rotate rapidly, free of any coupling between the stellar magnetic field and the disk (e.g., Preibisch 1999). From our high-resolution optical spectra (Sec. 2.3), we find that DoAr 21 is indeed a rapid rotator. There is also strong evidence for the presence of a disk, though perhaps not in the region immediately adjacent to the star.

The detection of H₂, possibly-accretion-related H α emission, and a strong mid-infrared excess around DoAr 21 calls the “diskless” interpretation into question. In the context of the x-ray observations presented here, it means that models of x-ray production that depend on star-disk interactions or on accretion (e.g. the “X-wind” model; Shu et al. 1997; Shang et al. 2002, or the models of Calvet & Gullbring 1998), as well as models that involve scaled-up coronal activity, are viable candidates for the x-ray emission from DoAr 21.

3.1. X-ray observations

The X-ray observations we report on in this paper were made with the *Chandra* X-Ray Telescope HETGS with the ACIS-S from 2003 May 5 to 2003 May 6, and have a total effective exposure time of 94 ks. The dispersed first order spectra are strong and continuum-dominated in both the HEG and MEG, as can be seen by a visual inspection of the ACIS chips, shown in Figure 8. There are no strong X-ray sources near enough to DoAr 21 to cause any contamination of the dispersed spectra.

PLACE FIG. 2 HERE: IMAGE OF DISPERSED SPECTRA ON CCD ARRAY

We centroided the zeroth order spectrum and determined that the standard spectral extractions were optimal and so used them for the analysis discussed here. The analysis was carried out in CIAO v2.3 using CALDB v2.26 (check ver number). (*David will refit at least some lines, using v3, and will update the preceding description.*) The spectral modeling and fitting was carried out using the *sherpa* software implemented in CIAO.

The spectra are dominated by strong, hard continuum emission. There are roughly three dozen emission lines detected superimposed on this continuum, ranging from Fe XXVI to Ne X. Due to the large interstellar column density, effectively no X-rays are detected longward of roughly 12 Å. We show the co-added first-order spectra (MEG and HEG) in Figure 9, with prominent lines labeled. The weakness of the lines relative to the continuum is due to the very high plasma temperatures, which leads to the nearly full ionization of most mid-Z elements, diminishing the line emission compared to the levels seen in solar-type coronal sources, and increasing the bremsstrahlung component. We separately model the global spectral properties, using multi-temperature thermal emission models, and individual lines and line complexes. We carried out these two different types of analysis in order to learn about the plasma kinematics (via line widths), the plasma temperature and elemental abundances (via global spectral fitting, with some constraints from individual line strengths), and the plasma density (via line ratios). We also investigate the time-variability properties of the X-rays, and note that a large X-ray flare was seen at roughly 50 ks into the observation. The X-ray light curve is shown in Figure 10.

PLACE FIGURE 3 HERE: FULL SPECTRUM OF DOAR 21; MEG and HEG.

PLACE FIGURE 4 HERE: FLARE

3.2. Global Fits to the X-ray Spectrum

The overall X-ray spectral energy distribution is governed primarily by the temperature distribution of the plasma and the amount of attenuation by cold gas, whether local to the star or along the interstellar sight line. Because of the very high temperature of the plasma on DoAr 21, most abundant ions are stripped, and there is relatively little line emission observed. The vast majority of the counts in the HEG and MEG spectra have their origin in the bremsstrahlung continuum component of the very hot plasma. By fitting multi-temperature thermal models with photoelectric absorption to both grating spectra, we can constrain the temperature distribution of the hot plasma, as well as the absorption

column density. This global fitting procedure also provides some constraints on the elemental abundances, mostly via line-to-continuum ratios. Because there are only a modest number of lines in the spectra, detailed element-by-element abundance determinations are not possible. Furthermore, the diagnostic information in the lines that are measured is best extracted by fitting the lines individually, which we discuss in the next section.

Our procedure was to fit the co-added negative and positive first-order MEG and HEG spectra simultaneously with APEC (Smith et al. 2001) thermal spectral models. We used both the C-statistic and the χ^2 statistic to assess goodness of fit (and determine confidence limits on the fitted parameters). The results we report on below as our best-fit model uses the χ^2 statistic, which is justified as the typical total counts per pixel is well above ten for this continuum-dominated source. Because this formal goodness of fit indicator is weighted by the number of counts, the quality of the fit to the continuum very strongly affected the derived model parameters. However, there is significantly more information in the emission line strengths than simply the number of counts would indicate. We thus used a second criterion, in addition to the χ^2 value, to assess how well each model fit the data. This second criterion was that the model reproduce the fluxes in the strongest dozen or so lines to within a factor of two.

We started with the simplest possible model, the isothermal model used to fit the low-resolution ACIS-I spectrum (Imanishi et al. 2002), and incrementally increased the complexity of the model until we achieved a good fit to the data. At each step we added additional free parameters and then more temperature components to the APEC model, going from an isothermal model with the temperature and mean abundance found by Imanishi et al. (2002) to an isothermal model with both temperature and abundance (as well as normalization) as free parameters. We next fit a two-temperature model and then a three-temperature model. In all cases the abundances were described by a single parameter, scaling the abundance of metals to that of hydrogen. Obviously, the metal abundance ratios are not exactly solar, and the temperature distribution in the plasma is continuous, rather than having a small number of discrete components. However, the quality of the spectra is not high enough to formally require a continuous temperature (differential emission measure, DEM) model or a model in which abundances were varied independently. It is good to keep in mind, however, that the multi-temperature components we find are likely approximations to peaks in the continuous DEM and the metallicity value we find is an average of various non-solar values for each abundant element.

We note that although we allowed the hydrogen column density to vary in each of our fits, each fit produced a value close to that corresponding to the 1.6 magnitudes of J-band extinction found by Luhman & Rieke (1999, see also Section 2.1). In each fit we froze the

neutral helium column density ratio at 0.1 and the ionized helium column density ratio at 0.01.

The results of the global fitting are summarized in Table 2. While the model used by Imanishi et al. (2002) does not fit the data well, the isothermal model with three free parameter generates a significantly improved, though not formally good, fit. The two-temperature model does provide a good fit, however, including reproducing nearly all of the emission line strengths to within a factor of 2. Adding a third temperature component does not further improve the fit, so we consider the two-temperature model to be our minimally complex good-fitting spectral model. The two temperatures bracket the single temperature fit to the ACIS-I spectrum by Imanishi et al. (2002). The abundances of each component are very similar and also close to the approximate mean value of 0.3 found from the ACIS-I fit.

We should note that the spectral fits we report on here are dominated by the flare in the middle of the observation. In section 3.4 we discuss the pre-flare spectral properties compared to those of the flare-state plasma. The pre-flare spectrum is indeed softer, as is usually seen in coronal sources where a flare event leads to additional plasma heating.

3.3. Model Fits to the Emission Lines

David’s comment/suggestions: Reiterate: strong continuum and weak lines (due to high T) Description of process here: MEG and/or HEG? Cstat (minimize for best-fit model...delta C for confidence limits)...1st order poly (fro continuum) ...but also tried brems...multiple Gaussians when there are other lines nearby...Gaussian params generally all treated as free (pos. as well as amp. and width)...[are there weak or blended lines where we froze pos? fwhm?]

Fig 3 too? refer to Fig 1 and labels

Discuss Si @ 6.18 Å in more detail, especially extra Gaussian used in test fit

Due to high temperatures, there is a strong continuum with weak emission lines in DoAr 21’s spectra. To determine the FWHM, amplitude, and position of these emission lines, we used Gaussian line shapes in CIAO. We fit the MEG and HEG spectra simultaneously, using the Cash statistic. In addition to the Gaussian line shape, we also fit a 1st order polynomial for the continuum, after trying a bremsstrahlung model, which we determined did not significantly affect the shape of the continuum. When there were several lines close to each other, we fit multiple Gaussians simultaneously. For weak lines where obtaining a good fit with all parameters free was problematic, we froze the position of the Gaussian line

model at the laboratory wavelength. Position uncertainties with a value of zero in Table 1 are values generated while freezing the position at zero. Generally, we treated the Gaussian parameters as free, varying position, amplitude, and width.

INSERT FIG 5: EXAMPLE OF STRONG EMISSION LINE HERE

Because we found the Si XIV emission line to be at least 2 sigma away from a line width velocity consistent with zero, while all other emission lines have FWHM velocities consistent with zero, we tried fitting various models to the Si XIV emission line. The Si XIV line is one of the strongest lines in our spectrum. We tried fitting an extra Gaussian, with its position fixed at 6.205 Å, to eliminate the possibility that a satellite emission line was causing the model broadening. With this model, we still found a width inconsistent with zero. We also determined the broadening could not be due to thermal broadening, as expected thermal broadening would cause a width as small as INSERT NUMBER HERE, while we find a width of INSERT NUMBER HERE. Using the chi squared statistic (*cvar*), we fit only the MEG spectrum (because the HEG had too few counts for the *cvar* statistic to be valid) allowing the width to be a free parameter, and then we froze the FWHM at zero. For our final results, quoted in Table 1, we used the single Gaussian model with a first order polynomial.

PLACE TABLE 1 HERE

3.4. X-ray Time Variability

The flare that occurred during our observation is shown in Figure 10, and analysis of the event is shown in Figure 11. As is typical for stellar flares, the ratio of hard to soft X-rays increases during the flare. To obtain further information about the flare event, we fit the two-temperature thermal model (the thermal model that most accurately described the entire spectrum) to the pre-flare, flare, and post-flare spectra. TALK ABOUT RESULTS HERE...AS SOON AS YOU HAVE THEM.

4. Discussion

The most surprising result from the new observations presented here is the large spatial extent of the 24- μ m emission from DoAr 21, which is puzzling to find around a cool star, and one with a very low millimeter flux. What this discovery has in common with the previous surprises about DoAr 21—the detections of PAH and H₂ emission—is that all of these observations are more commonly associated with more luminous, hotter stars. Here we explore whether it is possible to construct a model that explains all of the data, and we

focus in particular on trying to understand the influence of the nearby B2 V star HD 147889.

4.1. The FUV radiation field near DoAr 21

The ultraviolet flux from DoAr 21 itself is relatively poorly known. It was not detected by IUE (Valenti et al. 2003); examination of the archived IUE spectrum places a rough upper limit of $\sim 10^{-15}$ erg cm $^{-2}$ s $^{-1}$ at $\lambda = 2400\text{--}3200$ Å. Given the large extinction to DoAr 21 (roughly 11.6 magnitudes at $\lambda = 2500$ given our adopted visual extinction), however, the star could have an ultraviolet flux that is several orders of magnitude above its photospheric flux and it would not have been detected by IUE. Given its relatively low accretion rate, there is not independent evidence to suggest that DoAr 21 should have such a large UV excess.

The B2 V star HD 147889 lies at a projected distance of 0.4 pc from DoAr 21. At this distance, the ultraviolet flux reaching DoAr 21 from HD 147889 (assuming no attenuation) is roughly 0.6 erg cm $^{-2}$ s $^{-1}$ at $\lambda = 1000$ Å (Habart et al. 2003). This corresponds to $\chi \approx 400$, the flux expressed in units of 1.6×10^{-3} erg cm $^{-2}$ s $^{-1}$ (Habing 1968). In contrast, the FUV field from DoAr 21’s photosphere (estimated using a Kurucz model atmosphere and the stellar parameters given above) is $\chi \approx 0.075$ at a distance of $1 R_{\star}$ from the stellar surface and falls with distance from DoAr 21. Thus, unless DoAr 21 has a large undetected UV excess, it is likely that the emission from HD 147889 (which is relatively constant across the surface of DoAr 21’s disk) dominates the FUV field in the vicinity of DoAr 21.

We can estimate the effect of this flux on the emission from DoAr 21’s disk by considering models of circumstellar disks that include the effects of heating from UV radiation. The primary mechanisms for such heating are radiative excitation of H $_2$ followed by collisional de-excitation, and photoelectric ejection of electrons from dust grains.

4.2. What excites the PAH and H $_2$ emission?

However, recent work has shown that PAH grains that are larger and/or ionized can be excited by visible-light photons, consistent with the observation of PAH emission around some low-mass stars with relatively weak UV fluxes (Li & Draine 2002). Grain growth in DoAr 21’s disk could thus explain both the observed PAH emission and the presence of a gaseous disk (as seen in H $_2$) with little near-infrared excess (since larger grains have lower infrared continuum opacity).

One prediction of the Li & Draine (2002) model is that the spectrum of PAHs illuminated

by cool stars is different from that of those illuminated by hot stars. In particular, they predict that the $11.3 \mu\text{m}$ feature should be 2–3 times stronger than the $7.7 \mu\text{m}$ feature (when plotted as λF_λ) around cool stars, whereas the latter feature is stronger in regions of PAH emission illuminated by hotter stars. While we do not have a PAH spectrum of DoAr 21 that includes both of these features, it is possible to extract a spectrum for the bright ridge near DoAr 21 from the ISOCAM data; the spectrum is shown in Figure 7. The $7.7 \mu\text{m}$ feature is considerably stronger than the $11.3 \mu\text{m}$ feature, consistent with illumination by a source with significant UV flux. Thus, much of the PAH emission that is projected in the vicinity of DoAr 21 is likely illuminated by a hotter star. Upcoming observations with the IRS spectrograph on *Spitzer* should help resolve the question of whether there is substantial PAH emission excited by DoAr 21 itself.

5. Conclusions

We gratefully acknowledge the support of Chandra grant GO3-4021X, and support of the National Science Foundation through grant AST-0307830. We are grateful to Luisa Rebull, Karl Stapelfeldt, Michael Meyer, and Russel White for useful discussions. This research has made use of the SIMBAD database, operated at CDS, Strasbourg, France, and of NASA’s Astrophysics Data System.

REFERENCES

- André, P., Deeney, B. D., Phillips, R. B., & Lestrade, J. 1992, *ApJ*, 401, 667
- Argiroffi, C., Drake, J. J., Maggio, A., Peres, G., Sciortino, S., & Harnden, F. R. 2004, *ApJ*, 609, 925
- Bary, J. S., Weintraub, D. A., & Kastner, J. H. 2002, *ApJ*, 576, L73
- Bary, J. S., Weintraub, D. A., & Kastner, J. H. 2003, *ApJ*, 586, 1136
- Bontemps, S., et al. 2001, *A&A*, 372, 173
- Boulanger, F., et al. 2005, *A&A*, 436, 1151
- Bouvier, J. & Appenzeller, I. 1992, *A&AS*, 92, 481
- Bouvier, J., Bertout, C., & Bouchet, P. 1988, *A&AS*, 75, 1

- Buser, R., & Kurucz, R. L. 1992, *A&A*, 264, 557
- Calvet, N., & Gullbring, E. 1998, *ApJ*, 509, 802
- Casanova, S., Montmerle, T., Feigelson, E. D., & Andre, P. 1995, *ApJ*, 439, 752
- D'Antona, F., & Mazzitelli, I. 1997, *Memorie della Societa Astronomica Italiana*, 68, 807
- de Zeeuw, P. T., Hoogerwerf, R., de Bruijne, J. H. J., Brown, A. .G. A., & Blaauw, A. 1999, *AJ*, 117, 354
- Dolidze, M. V. & Arakelyan, M. A. 1959, *Soviet Ast.*, 3, 434
- Feigelson, E. D. & Montmerle, T. 1985, *ApJ*, 289, 19
- Feigelson, E. D. & Montmerle, T. 1999, *ARA&A*, 37, 363
- Feigelson, E. D., Garmire, G. P., & Pravdo, S. H. 2002, *ApJ*, 572, 335
- Fernández, M., et al. 2004, *A&A*, 427, 263
- Fitzpatrick, E. L. 1999, *PASP*, 111, 63
- Gagné, M., Skinner, S. L., & Daniel, K. J. 2004, *ApJ*, 613, 393
- Habart, E., Boulanger, F., Verstraete, L., Pineau des Forêts, G., Falgarone, E., & Abergel, A. 2003, *A&A*, 397, 623
- Habing, H. J. 1968, *Bull. Astron. Inst. Netherlands*, 19, 421
- Hanner, M. S., Brooke, T. Y., & Tokunaga, A. T. 1995, *ApJ*, 438, 250
- Haro, G. 1949, *AJ*, 54, 188
- Herczeg, G. J., Wood, B. E., Linsky, J. L., Valenti, J. A., & Johns-Krull, C. M. 2004, *ApJ*, 607, 369
- Hines, D.C. et al. 2005, “FEPS Data Explanatory Supplement,” Version 2.1, (Pasadena: SSC)
- Igea, J. & Glassgold, A. E. 1999, *ApJ*, 518, 848
- Imanishi, K., Tsujimoto, M., & Koyama, K. 2002, *ApJ*, 572, 300
- Imanishi, K., Nakajima, H., Tsujimoto, M., Koyama, K., & Tsuboi, Y. 2003, *PASJ*, 55, 653

- Jensen, E. L. N., Mathieu, R. D., Donar, A. X., & Dullighan, A. 2004, *ApJ*, 600, 789
- Kamata, Yuichi, Koyama, Katsuji, Tsuboi, Yohko, & Yamauchi, Shigeo 1997, *PASJ*, 49, 461
- Kastner, J. H., Huenemoerder, D. P., Schulz, N. S., Canizares, C. R., & Weintraub, D. A. 2002, *ApJ*, 567, 434
- Kastner, J. H., Huenemoerder, D. P., Schulz, N. S., Canizares, C. R., Li, Jingqiang, & Weintraub, D. A. 2004, *ApJ*, 605, 49
- Keenan, P. C., & McNeil, R. C. 1989, *ApJS*, 71, 245
- Koerner, D. W., Jensen, E. L. N., Cruz, K. L., Guild, T. B., & Gultekin, K. 2000, *ApJ*, 533, L37
- Koyama, Katsuji, Maeda, Yoshitomo, Ozaki, Masanobu, Ueno, Shiro, Kamata, Yuichi, Tawara, Yuzuru, Skinner, Stephen, & Yamauchi, Shigeo 1994, *PASJ*, 46, 125
- Massarotti, A., Latham, D. W., Torres, G., Brown, R. A., & Oppenheimer, B. D. 2005, *AJ*, 129, 2294
- Lada, C. J. & Wilking, B. A. 1984, *ApJ*, 287, 610
- Li, A., & Draine, B. T. 2002, *ApJ*, 572, 2
- Luhman, K. L. & Rieke, G. H. 1999, *ApJ*, 525, 440
- Maloney, P. R., Hollenbach, D. J., & Tielens, A. G. G. M. 1996, *ApJ*, 466, 561.
- Martín, E. L., Montmerle, T., Gregorio-Hetem, J., & Casanova, S. 1998, *MNRAS*, 300, 733
- Martin, P. G., et al. 1992, *ApJ*, 392, 691
- Montes, D., Fernandez-Figueroa, M. J., de Castro, E., & Sanz-Forcada, J. 1997, *A&AS*, 125, 263
- Montmerle, T., Koch-Miramond, L., Falgarone, E., & Grindlay, J. E. 1983, *ApJ*, 269, 182
- Okumura, K., Prault, M., & Longval, Y. 1998, technical report, Ghosts in ISOCAM images (http://www.iso.vilspa.esa.es/users/expl_lib/CAM_list.html)
- Palla, F., & Stahler, S. W. 1999, *ApJ*, 525, 772
- Phillips, R. B., Lonsdale, C. J., & Feigelson, E. D. 1991, *ApJ*, 382, 261

- Preibisch, T. 1999, *A&A*, 345, 583
- Romaniello, M., Robberto, M., & Panagia, N. 2004, *ApJ*, 608, 220
- Rydgren, A. E., & Vrba, F. J. 1983, *ApJ*, 267, 191
- Sanz-Forcada, J., Maggio, A., & Micela, G. 2003, *A&A*, 408, 1087
- Schmidt-Kaler Th., 1982, *Landolt Börnstein Catalogue*, Vol. VI/2b
- Schmitt, J. H. M. M., Robrade, J., Ness, J.-U., Favata, F., & Stelzer, B. 2005, *A&A*, 432, L35
- Shang, H., Glassgold, A. E., Shu, F. H., & Lizano, S. 2002, *ApJ*, 564, 853
- Shu, F. H., Shang, H., Glassgold, A. E., & Lee, T. 1997, *Science*, 277, 1475
- Siess, L., Dufour, E., & Forestini, M. 2000, *A&A*, 358, 593
- Smith, R. K., Brickhouse, N. S., Liedahl, D. A., & Raymond, J. C. 2001, *ApJ*, 556, L91
- Stapelheldt, K. R., et al. 2005, in preparation
- Stelzer, B. & Schmitt, J. H. M. M. 2004, *A&A*, 418, 687
- Stine, P. C., Feigelson, E. D., Andre, P., & Montmerle, T. 1988, *AJ*, 96, 1394
- Valenti, J. A., Basri, G., & Johns, C. M. 1993, *AJ*, 106, 2024
- Valenti, J. A., Fallon, A. A., & Johns-Krull, C. M. 2003, *ApJS*, 147, 305
- Vrba, F. J., Coyne, G. V., & Tapia, S. 1993, *AJ*, 105, 1010
- Vuong, M. H., Montmerle, T., Grosso, N., Feigelson, E. D., Verstraete, L., & Ozawa, H. 2003, *A&A*, 408, 581
- Weaver, W. B., & Jones, G. 1992, *ApJS*, 78, 239
- Weintraub, D. A., Saumon, D., Kastner, J. H., & Forveille, T. 2000, *ApJ*, 530, 867
- White, R. J., & Basri, G. 2003, *ApJ*, 582, 1109
- White, R. J., & Ghez, A. M. 2001, *ApJ*, 556, 265

Table 1. Fits to Individual Emission Lines

Ion	λ_{lab} (Å)	λ_{obs} (Å)	Flux (10^{-5} photons $\text{s}^{-1}\text{cm}^{-2}$)	FWHM (km s^{-1})
Fe XXVI	1.7798	1.7798	$0.949^{+0.376}_{-0.323}$	98^{+1476}_{-98}
Fe XXV	1.8504 ± 0.0006	1.8504	$2.014^{+0.461}_{-0.415}$	241^{+4214}_{-241}
Ca XX	2.5494 ± 0.00001	2.5494	$0.320^{+0.097}_{-0.316}$	0
Ca XX	3.0203 ± 0.00002	3.0203	$0.897^{+0.297}_{-0.275}$	2494^{+1462}_{-1180}
Ca XIX	3.1772	3.1772	$0.358^{+0.186}_{-0.165}$	0
Ar XVII	3.9491	3.9491	$0.530^{+0.210}_{-0.187}$	78^{+1012}_{-78}
S XVI	3.9912 ± 0.00002	3.9912	$0.185^{+0.171}_{-0.146}$	0
S XVI	4.7292 ± 0.00002	$4.73395^{+0.0010}_{-0.0016}$	$0.898^{+0.195}_{-0.181}$	74^{+420}_{-74}
S XV	5.0387 ± 0.002	5.0387	$1.000^{+0.277}_{-0.247}$	37^{+947}_{-37}
S XV	5.0631 ± 0.002	5.0631	$0.343^{+0.210}_{-0.178}$	36^{+631}_{-36}
S XV	5.1015 ± 0.002	5.1015	$0.503^{+0.224}_{-0.193}$	36^{+412}_{-36}
Si XIV	6.1823 ± 0.0003	6.182 ± 0.0009	$1.96^{+1.09}_{-0.184}$	458^{+119}_{-120}
Ni XXVI	6.3392 ± 0.005	$6.3499^{+0.0029}_{-0.0026}$	$0.244^{+0.106}_{-0.095}$	48^{+1318}_{-48}
Si XIII	6.6479 ± 0.002	$6.648^{+0.0021}_{-0.0024}$	$0.510^{+0.134}_{-0.133}$	220^{+505}_{-220}
Si XIII	6.685 ± 0.002	$6.685^{+0.0028}_{-0.0034}$	0.329 ± 0.117	204^{+730}_{-204}
Si XIII	6.7403 ± 0.002	$6.741^{+0.0063}_{-0.0017}$	0.548 ± 0.119	216^{+282}_{-216}
Mg XII	7.1062 ± 0.00004	$7.102^{+0.0047}_{-0.0048}$	$0.260^{+0.0793}_{-0.0750}$	396^{+580}_{-396}
Al XIII	7.1728 ± 0.00004	$7.1674^{+0}_{-0.0024}$	$0.251^{+0.071}_{-0.067}$	31^{+738}_{-31}
Fe XXIII	7.4780 ± 0.002	$7.485^{+0.0049}_{-0.0014}$	$0.176^{+0.070}_{-0.0655}$	54^{+1053}_{-54}
Mg XI	7.8503 ± 0.002	$7.854^{+0.0024}_{-0.0038}$	$0.166^{+0.0640}_{-0.0591}$	66^{+273}_{-66}
Al XII	7.8721 ± 0.0003	7.8721	$0.0418^{+0.0572}_{0.0521}$	0
Fe XXIV	7.9857	7.9857	$0.208^{+0.0784}_{-0.0703}$	11^{1025}_{-11}
Fe XXIV	8.2326	8.2326	$0.175^{+0.0874}_{-0.0769}$	17^{+2608}_{-16}
Mg XII	8.4203 ± 0.0001	$8.420^{+0.0021}_{-0.0003}$	0.748 ± 0.142	25^{+317}_{-25}
Ne X	9.4797	$9.480^{+0.0060}_{-0.0050}$	0.342 ± 0.124	585^{+616}_{-509}
Ne X	9.7082 ± 0.00005	9.710 ± 0.0049	0.0203 ± 0.107	28^{+955}_{-28}
Fe XIX	9.8188	9.800 ± 0.0043	0.200 ± 0.102	135^{+789}_{-135}
Ni XXIV	9.97 ± 0.006	$9.875^{+0.0063}_{-\infty}$	0.159 ± 0.102	15^{+170}_{-15}
Ne X	10.2388 ± 0.00005	$10.236^{+0.0011}_{-0.0014}$	$0.421^{+0.084}_{-0.077}$	26^{+277}_{-26}
Fe XVIII	10.3603	10.3603	$0.1440^{+0.0637}_{-0.0560}$	302^{+329}_{-302}

Table 1—Continued

Ion	λ_{lab} (Å)	λ_{obs} (Å)	Flux (10^{-5} photons $\text{s}^{-1}\text{cm}^{-2}$)	FWHM (km s^{-1})
Fe XXIV	10.619 ± 0.02	$10.622^{+0.0028}_{-0.0018}$	$0.347^{+0.0790}_{-0.0711}$	24^{+127}_{-24}
Fe XXIV	10.6630 ± 0.005	$10.66^{+0.0018}_{-0.0008}$	$0.0244^{+0.0726}_{-0.0642}$	35^{+318}_{-35}
Fe XXIII	10.981 ± 0.003	$10.980^{+0.0425}_{-0.0084}$	0.135 ± 0.130	118^{+20078}_{-118}
Fe XXIII ¹ and Fe XXIV ²	11.024 ± 0.003	$11.030^{+0.0048}_{-0.0051}$	0.260 ± 0.139	36^{+854}_{-36}
Fe XXIII	11.736 ± 0.004	$11.736^{+0.0050}_{-0.0055}$	0.287 ± 0.171	102^{+555}_{-102}
Fe XXII	11.77 ± 0.003	11.77	$0.1408^{+0.0580}_{-0.0468}$	1^{640}_{-1}
Ne X and Fe XVIII	12.131 ± 0.0001	12.131	$0.272^{+0.092}_{-0.079}$	242^{+17}_{-19}
Fe XXI	12.2840 ± 0.002	12.2840	$0.259^{+0.105}_{-0.088}$	5^{+838}_{-5}

¹11.019 Å

²11.029 Å

Table 2. Thermal Model Fit Parameters

Model	N_{H} (cm^{-2})	kT (keV)	Abundance (solar units)	Emission Measure 10^{12}cm^{-5}	Fit Probability
Imanishi	1e22 (frozen)	2.9 (frozen)	0.3 (frozen)	2.1 ± 0.02	1.90×10^{-4}
1-Temperature	$8.32 \pm 0.01 \times 10^{21}$	$6.94^{+0.06}_{-0.04}$	0.84 ± 0.03	1.9 ± 0.02	0.111
2-Temperature	$1.24 \pm 0.01 \times 10^{22}$	-----	-----	-----	0.880
component 1	-----	$1.489^{+0.038}_{-0.037}$	0.260 ± 0.014	1.1 ± 0.03	-----
component 2	-----	$5.626^{+0.211}_{-0.206}$	0.322 ± 0.037	0.012 ± 0.020	-----
3-Temperature	$1.22 \pm 0.01 \times 10^{22}$	-----	-----	-----	0.867
component 1	-----	2.435 ± 0.046	0.277 ± 0.017	1.6 ± 0.02	-----
component 2	-----	$0.777^{+0.043}_{-0.042}$	$1.5^{+0.153}_{-0.135}$	$0.09^{+0.008}_{-0.007}$	-----
component 3	-----	$11.926^{+1.780}_{-1.493}$	$0.633^{+0.121}_{-0.120}$	$0.6^{+0.01}_{-0.01}$	-----

Table 3. Two Temperature model Fit Parameters to Flare and Quiescent Spectra

Model	N_{H} (cm^{-2})	kT (keV)	Abundance (solar units)	Normalization (10^{12}cm^{-5})	Fit Probability
Quiescent	1.17×10^{22} (frozen)	-----	0.281 ± 0.020	-----	1.00
component 1	-----	0.978 ± 0.063	-----	0.4 ± 0.004	-----
component 2	-----	2.813 ± 0.089	-----	1.2 ± 0.02	-----
Flare	1.17×10^{22} (frozen)	-----	0.459 ± 0.033	-----	1.00
component 1	-----	1.507 ± 0.098	-----	0.9 ± 0.06	-----
component 2	-----	$5.811^{+0.353}_{-0.354}$	-----	2.1 ± 0.04	-----

Fig. 8.— Image of the dispersed HETGS spectra on the ACIS CCD array. The zeroth order spectrum can be seen as a bright point source, with four lines in a shallow X pattern centered on it. The arms of the X pattern are the negative and positive first order dispersed spectra from the MEG and HEG arrays. It can be seen from this image that the dispersed spectra in both the MEG and HEG are strong, and dominated by continuum emission. It can further be seen that there are no other bright point sources contaminating the dispersed spectra of Do Ar 21.

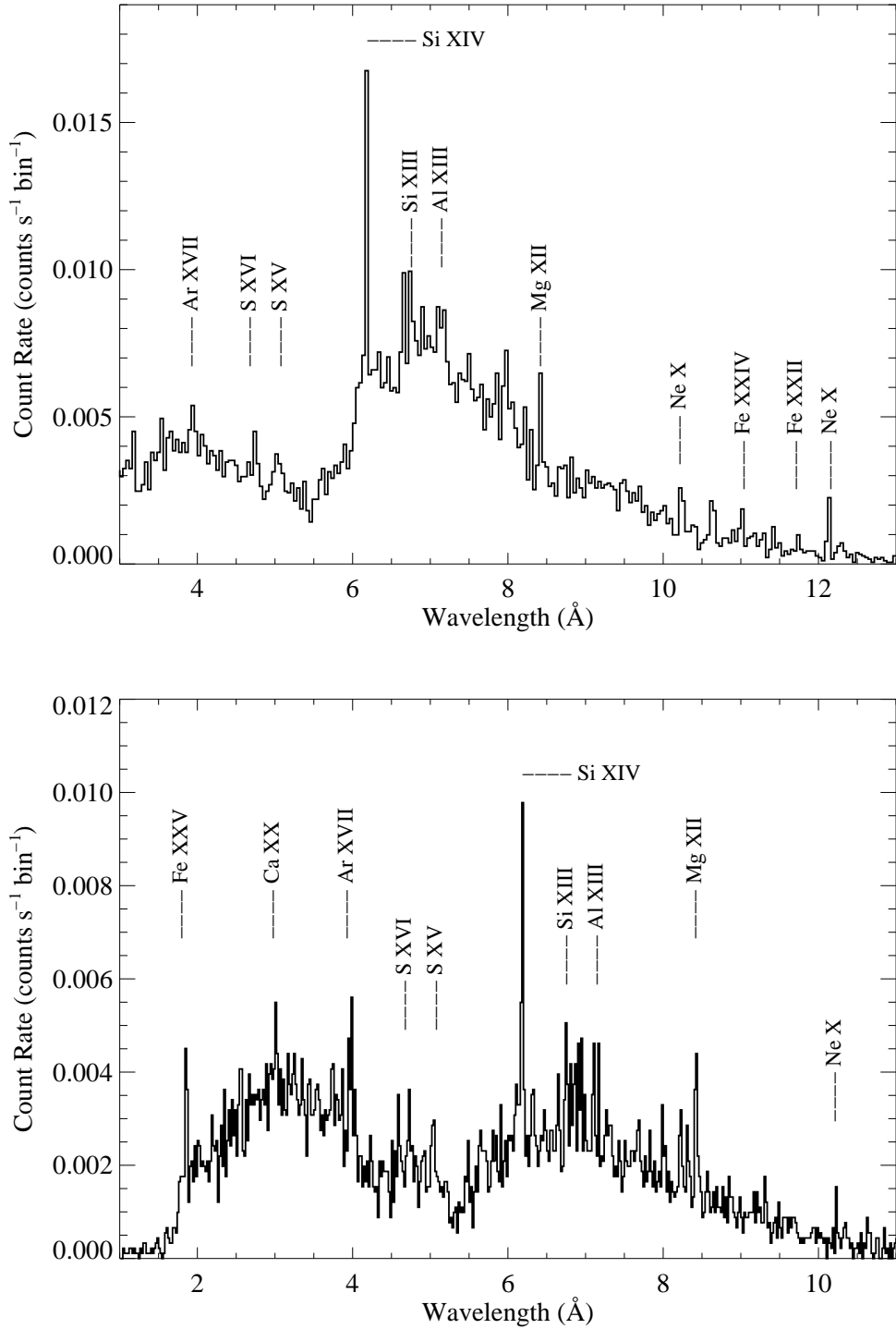


Fig. 9.— The MEG spectrum (top) and HEG spectrum (bottom). Both spectra have been binned by a factor of eight (for the MEG, the bin size is 0.025 Å; for the HEG, the bin size is 0.0125 Å) and the strong emission lines are labeled. The shape of the continuum, a primarily multi-temperature bremsstrahlung, is governed by the HETGS effective area.

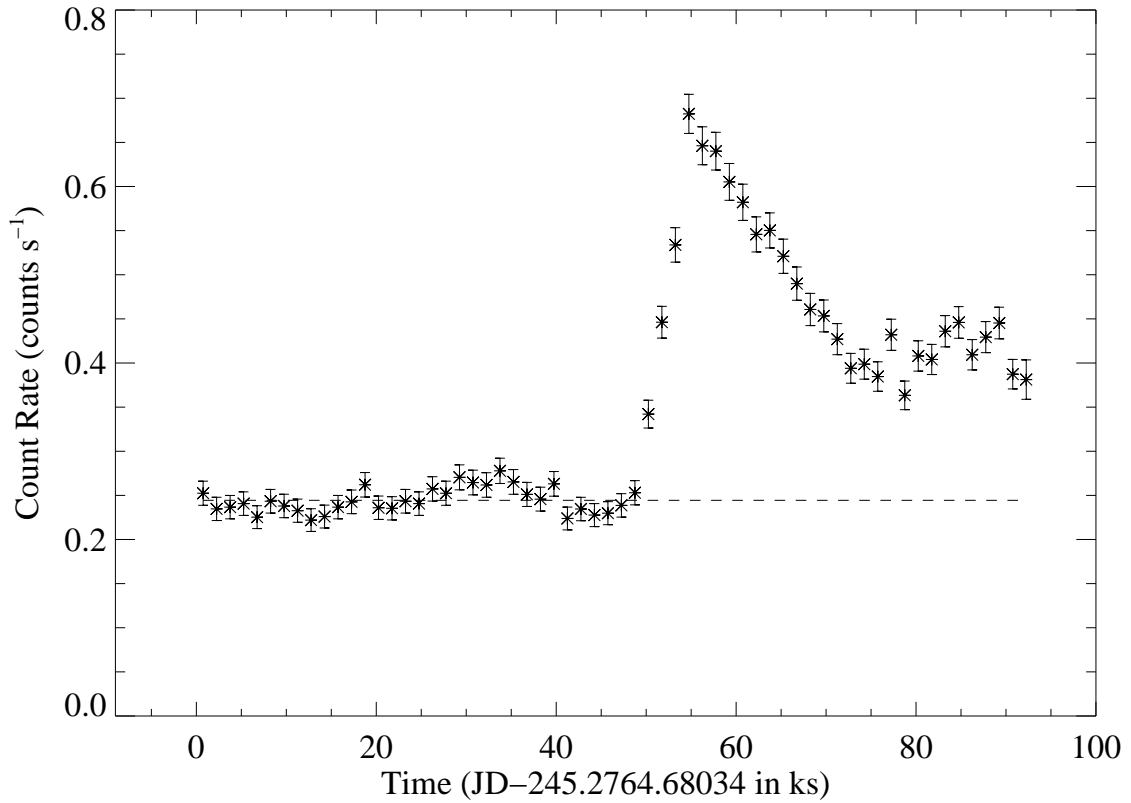


Fig. 10.— The light curve of DoAr 21, clearly showing the flare that occurred at roughly 50 ks into our observation. The bin size of the light curve is 1500 s and the dashed line represents the average count rate for the quiescent phase.

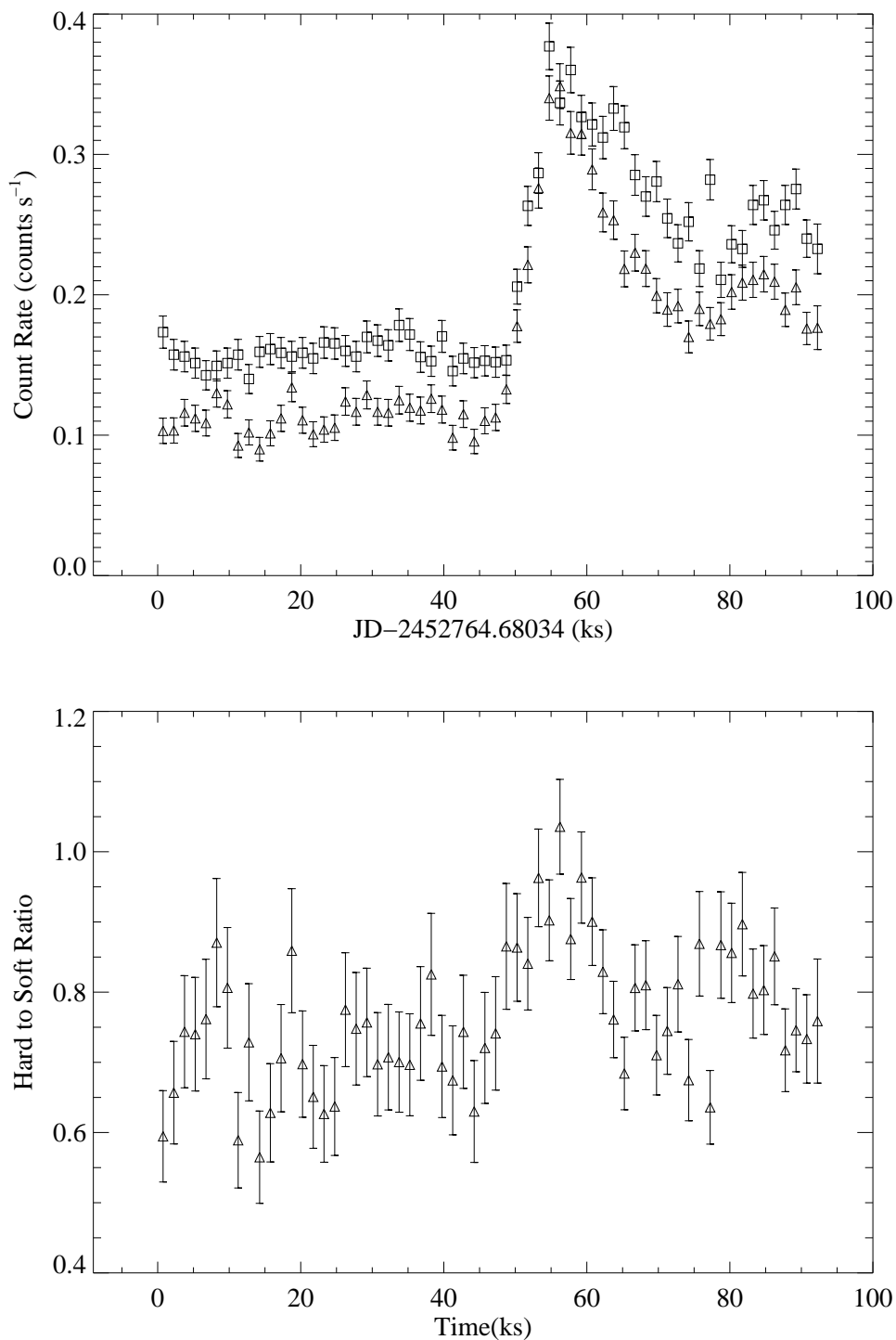


Fig. 11.— The hard and soft x-ray lightcurves (1500 s bin size) plotted together (top). The hard X-rays (from 1.5 to 6 Å) are represented by triangles while the soft X-rays (from 6 to 20 Å) are represented by squares. The ratio of hard to soft X-rays is shown in the bottom panel. It is clear that the X-rays harden during the flare but relatively quickly revert back to the pre-flare ratio.

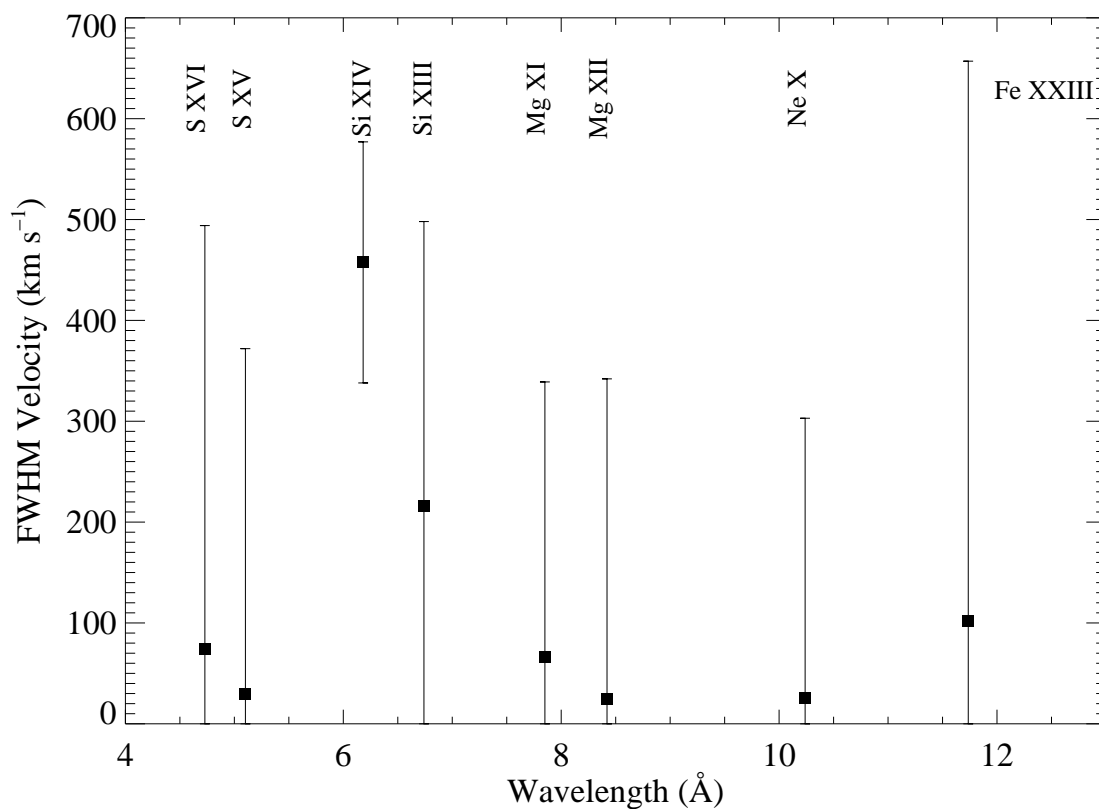


Fig. 12.— Best-fit emission line widths (FWHM) of the strongest lines in the HETGS spectra, along with their 68 % confidence limits. Although only the Si XIV Lyman- α line has a width inconsistent with zero, the entire ensemble of lines is consistent with a mean broadening of $v_{\text{FWHM}} \approx 300 \text{ km s}^{-1}$.

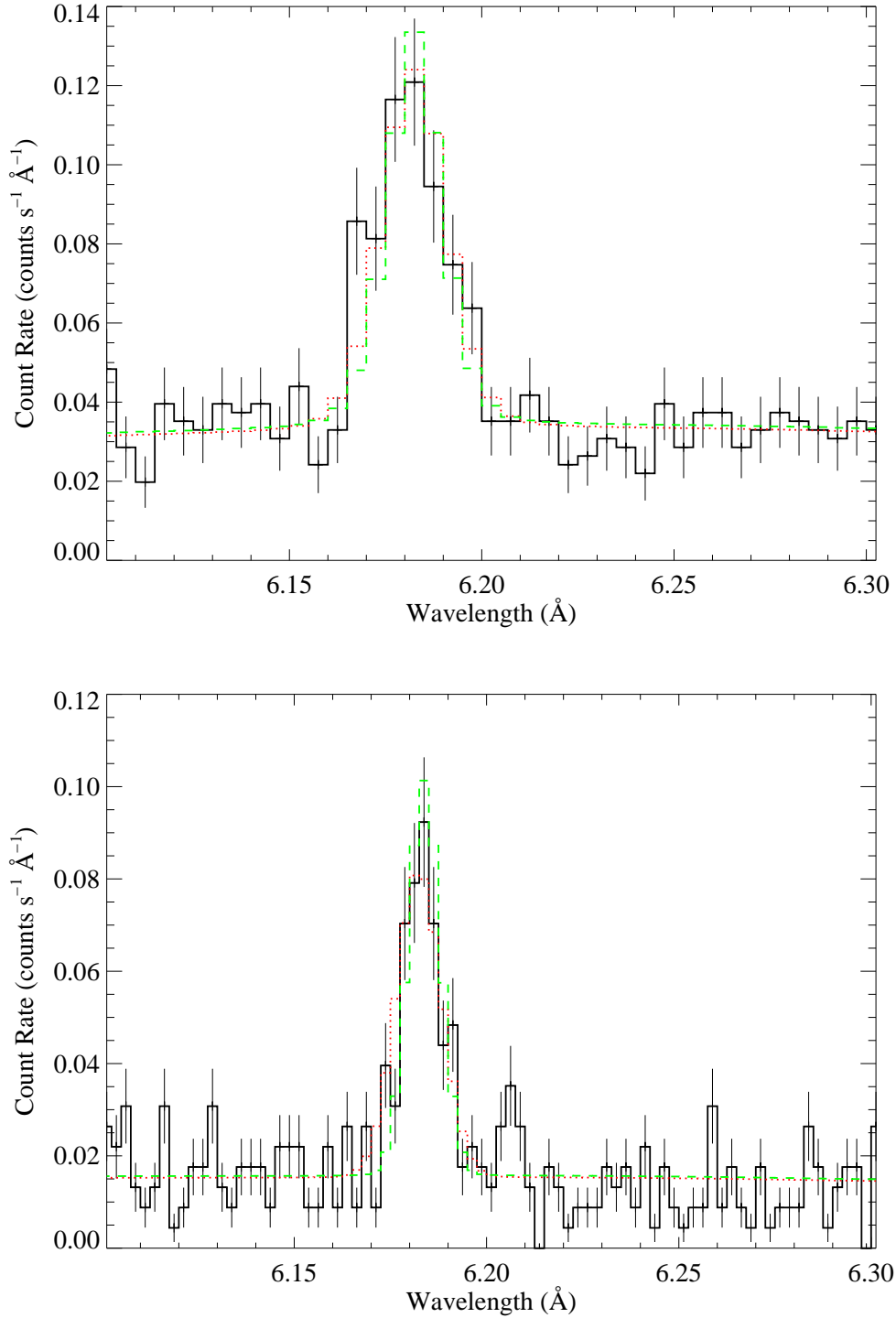


Fig. 13.— The Si XIV Lyman- α line is the strongest emission line in the HETGS spectrum. It shows evidence of modest Doppler broadening. We show this line in the MEG (top) and HEG (bottom) with the best-fit Gaussian model (convolved with the instrumental response function) in red. An intrinsically narrow model (also convolved with the instrumental response function) is shown in green. The moderately broadened model is a statistically better fit than the narrow model (which is ruled out at the 3 sigma level).

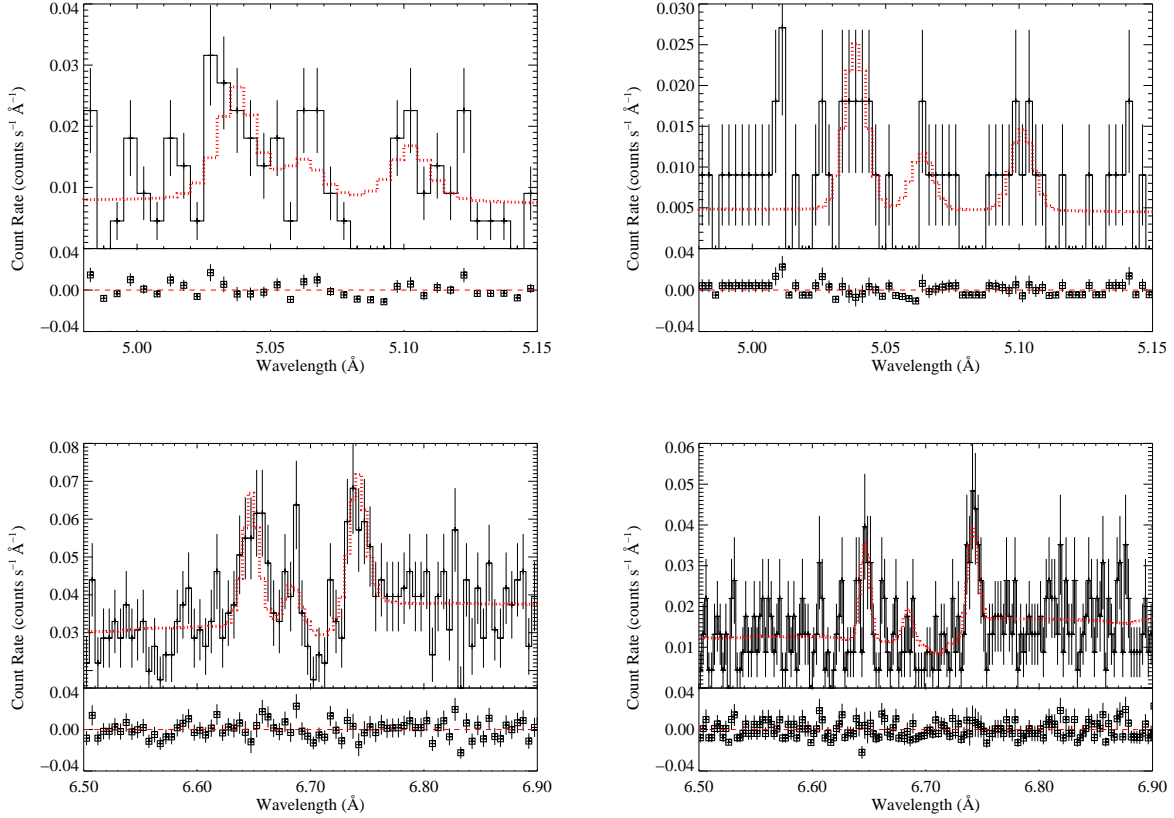


Fig. 14.— The S XV (top) and Si XIII (bottom) $f - i - r$ complexes as measured in the MEG (left) and HEG (right). The model is the dashed line (colored red in the online edition) plotted over the data (black histogram with Poisson uncertainties indicated by the vertical lines). The resonance, intercombination, and forbidden lines are indicated by the r , i , and f labels, respectively. Residuals from the displayed best-fit models are shown in the lower part of each panel.